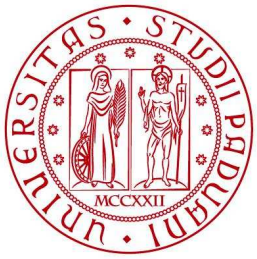

UNIVERSITÀ
DEGLI STUDI
DI PADOVA

Sede Amministrativa: Università degli Studi di Padova
Dipartimento di Fisica e Astronomia

SCUOLA DI DOTTORATO DI RICERCA IN: ASTRONOMIA
CICLO: XXV

STUDY OF THE PROPAGATION AND DETECTION OF THE ORBITAL ANGULAR MOMENTUM OF LIGHT FOR ASTROPHYSICAL APPLICATIONS

Direttore della Scuola:	Ch.mo Prof. Giampaolo Piotto
Supervisore:	Ch.mo Prof. Antonio Bianchini
Correlatori:	Ch.mo Prof. Cesare Barbieri Dott. Fabrizio Tamburini

Dottoranda: Anna Sponselli

Gennaio 2013

By striving to do the impossible, man has always achieved what is possible. Those who have cautiously done no more than they believed possible have never taken a single step forward.

M. Bakunin

Acknowledgements

I want to thank all the people who have taught, helped and stimulated me during my PhD.
I have to thank Fabrizio Tamburini, who talked to me about the orbital angular momentum of light for the first time in 2006, opening a new word in my mind with his ideas and allowing me to focus my studies and research on topics that thrill me so much. It is his credit or fault if my bachelor thesis, master thesis and now PhD thesis have been focused on this subject!
It is a pleasure for me to thank Bo Thidé: his way to approach science has transmitted me a great sense of excitement for science and professional responsibility, intellectual honesty combined with great passion.
A special thank is for Cesare Barbieri, for having always supported and stimulated me: with his example, he has taught me the importance and beauty of curiosity.
I am grateful to Antonio Bianchini, who has hosted me in his office several times and has always been helpful when necessary.

I want to acknowledge professor Miles Padgett, for having accepted me in his group for three highly instructive months, allowing me to try the experimental side of science: thanks to him, I have realized further the deep meaning and essential role of testing.
I am particularly grateful to Martin Lavery, who has thought me everything I know about an optical laboratory and the great patience required.

I am indebted with all these persons, for having shown me that whatever is your choice, the driving force has to be passion.

Abstract

The aim of this work is to study the propagation of orbital angular momentum (OAM) of light for astrophysical applications and a method for OAM detection with optical telescopes.
The thesis deals with the study of the orbital angular momentum (OAM) as a new observable for astronomers, which could give additional information with respect to those already inferred from the analysis of the intensity, frequency and polarization of light. Indeed, the main purpose of this work is to highlight that light can have a much more complex structure, and therefore can transport much more information.
In particular, firstly we show that OAM can be imparted to light from interstellar media with a perturbed electron density function in the plane perpendicular to the propagation direction, revealing that the study of OAM could give information about the spatial structures of the traversed inhomogeneous media.
The second part of the thesis deals with an experimental verification of the preservation of orbital angular momentum even for uncorrelated non-monochromatic wave beams, showing that this observable of light is preserved, thus we can aim at detecting it.
Finally, if OAM can transport information, and if it is preserved in propagation, the obvious consequence is the study of its detection, in particular by an OAM mode sorter fitted to optical telescopes.

Contents

Riassunto

La radiazione elettromagnetica trasporta energia e momento. Solitamente il momento trasportato dalla luce viene associato al *momento lineare*, responsabile della pressione di radiazione e associato all'azione di una forza. Tuttavia vi è un'altra componente del momento, il *momento angolare*: esso è associato all'azione di un un momento torcente e, in certe condizioni, può essere approssimato alla somma vettoriale del *momento angolare di spin* e del *momento angolare orbitale* (OAM). Il momento angolare di spin è la componente più conosciuta del momento angolare, ed è associato all'elicità destrogira o levogira del fascio di luce, perciò è connesso al concetto di polarizzazione. Recenti studi hanno evidenziato l'importanza anche del momento angolare orbitale della luce. Quest'ultimo è associato a una forma elicoidale del fronte d'onda, causata dalla precessione del vettore di Poynting attorno alla direzione di propagazione del fascio di luce. Questo nuovo osservabile del campo elettromagnetico trova diverse applicazioni nella fisica (sia sperimentale che teorica) e nell'astrofisica, aprendo nuovi scenari all'astronomia. Il momento angolare orbitale trova un uso pratico in molti campi: nelle tecnologie radar, nelle nanotecnologie, negli esperimenti quantistici, nell'informazione quantistica etc. [25, 57]; in astronomia viene sfruttato per migliorare il potere risolutivo degli strumenti ottici altrimenti limitati dalla diffrazione [77], e per facilitare il rilevamento di pianeti extrasolari tramite l'utilizzo del coronografo a vortici ottici [8, 24, 40, 41, 46, 49, 82]. Alcuni lavori teorici dimostrano che l'OAM potrebbe essere usato come un nuovo strumento diagnostico per lo studio di campi gravitazionali rotanti, ad esempio i buchi neri di Kerr [81], e che potrebbe fornire informazioni riguardo la struttura spaziale del mezzo attraversato dai fotoni durante il loro viaggio dalla sorgente all'osservatore [80].

In questa tesi vengono studiati la propagazione del momento angolare orbitale della luce per applicazioni astrofisiche, e un possibile metodo per il rilevamento dell'OAM con i telescopi ottici. Lo scopo principale di questo

lavoro è quello di evidenziare che la luce può avere una struttura molto più complessa di quello che solitamente credono gli astronomi, e perciò che può trasportare molta più informazione. In particolare, in questa tesi il momento angolare obitale della luce viene trattato come un nuovo osservabile per gli astronomi, che potrebbe dare informazioni aggiuntive rispetto a quelle che già si deducono dall'analisi dell'intensità, della frequenza e della polarizzazione della luce.

Nel capitolo 1 introduciamo il concetto di momento angolare orbitale della radiazione elettromagnetica (e, nel limite quantistico, dei fotoni).
Se consideriamo un fascio di luce laser polarizzata, esso trasporta OAM quando il campo elettrico in coordinate cilindriche (r, θ, z) ha la seguente forma:

$$\vec{E}(\vec{r}, t) = \widehat{\sigma} u(r, \theta, z) e^{i(kz - wt)} + c.c.$$

dove $\widehat{\sigma}$ è il versore della polarizzazione, *c.c.* rappresenta il complesso coniugato e la funzione complessa $u(r, \theta, z)$ è la funzione che descrive il profilo di ampiezza del campo, ed è definita come:

$$u(r, \theta, z) = u_0(r, z) e^{i\ell\theta}.$$

Notiamo che la fase totale del campo ha acquisito una nuova componente, adesso troviamo che:
$fase\ dell'\ onda = kz - wt + \ell\theta$.
La componente $\ell\theta$, dove θ è un angolo, è la fase azimutale: è a causa della presenza di questa componente azimutale che nasce il momento angolare orbitale e che il fronte d'onda acquisisce una forma elicoidale che si avvolge attorno all'asse di propagazione [3, 62]. Il contributo orbitale è determinato solamente dalla dipendenza da una fase azimutale, e è equivalente a $\ell\hbar$ per fotone. Consideriamo un fascio di luce caratterizzato da un determinato valore intero di ℓ. In un piano perpendicolare alla direzione di propagazione, la fase è sottoposta ℓ volte a una variazione di 2π, e lungo l'asse di propagazione appare una singolarità di fase. L'interferenza distruttiva che ha luogo lungo tale singolarità dà origine a un profilo di intensità a forma di anello.
Un fascio di Laguerre-Gauss, ben conosciuto nell'ottica parassiale, è un esempio fisico facilmente realizzabile della luce con questa distribuzione di fase.

Nel capitolo 2 analizziamo il meccanismo di acquisizione di massa di Anderson-Higgs per un fotone in un plasma, e studiamo il contributo a tale massa dato dal momento angolare orbitale acquisito da un fascio di fotoni quando attraversa una distribuzione di cariche con una certa struttura spaziale. A questo fine applichiamo le equazione di Proca al caso di un plasma statico con una particolare distribuzione spaziale delle cariche

libere, nello specifico un vortice, in grado di imporre momento angolare orbitale alla luce. Troviamo che, in aggiunta alla massa acquisita attraverso il tradizionale meccanismo di Anderson-Higgs, il fotone acquisisce un'ulteriore massa connessa al momento angolare orbitale che riduce la massa del fotone prevista dalle equazioni di Proca. In questo modo mostriamo che un fotone acquisisce OAM ogni volta che attraversa un mezzo che, nel piano perpendicolare alla direzione di propagazione del fascio, è caratterizzato da una densità con una componente azimutale non omogenea. Dato che questo OAM dipende dalla distribuzione spaziale delle cariche (nel piano perpendicolare alla direzione di propagazione), esso potrebbe essere sfruttato in astronomia per ottenere informazioni riguardanti la struttura spaziale dei mezzi attraversati dalla radiazione elettromagnetica. Perciò il momento angolare orbitale potrebbe essere utilizzato dagli astronomi come nuovo strumento di diagnosi: lo studio dell'OAM della luce catturata dai nostri telescopi potrebbe infatti darci informazioni aggiuntive riguardanti la funzione di densità del mezzo interstellare attraversato dai fotoni.
I risultati trattati in questo capitolo si possono trovare nella pubblicazione "*Photon orbital angular momentum and mass in a plasma vortex*" [80].

Nel capitolo 3 riportiamo i risultati di alcuni esperimenti condotti nel mondo reale, all'aperto, riguardanti lo studio della propagazione del momento angolare orbitale nelle frequenze radio: dato che l'OAM è una proprietà del campo elettromagnetico, ha lo stesso comportamento a tutte le frequenze. In questi esperimenti abbiamo generato e propagato onde radio non monocromatiche, con diversi valori di OAM, per trasmettere simultaneamente due canali radio sulla stessa frequenza, codificati con diversi stati OAM ($\ell = 0$ e $\ell = 1$). Il risultato positivo di questi esperimenti dimostra che:

- onde non monocromatiche, incoerenti (quindi interessanti nel campo dell'astronomia, poichè è il principale tipo di luce che gli astronomi ricevono), preservano l'impronta del loro momento angolare orbitale anche nel far field;

- gli stati OAM sono stati ortogonali, cioè stati che non si influenzano reciprocamente, e la loro ortogonalità è preservata.

Da un punto di vista astronomico, ciò significa che il messaggio trasportato dalla luce può arrivare a noi e che noi possiamo quindi cercare di misurarlo.
I risultati descritti in questo capitolo si possono trovare nella pubblicazione "*Encoding many channels on the same frequency through radio vorticity: first experimental test*" [78].

Se l'OAM può essere un nuovo osservabile astronomico in grado di trasportare informazioni astrofisiche, e se queste informazioni si preservano durante la propagazione, il passo successivo è cercare di misurare l'OAM racchiuso nella luce raccolta dai telescopi astronomici. Finora l'OAM contenuto nella luce proveniente da oggetti astrofisici non è mai stato misurato. Nel capitolo 4 descriviamo un possibile modo per misurarlo con i telescopi ottici, utilizzando il cosiddetto *OAM mode sorter* [15, 16, 43, 44], uno strumento in grado di misurare lo spettro OAM. Tale dispositivo finora è stato usato sui banchi ottici con luce laser, e noi lo abbiamo adattato in modo da poter essere utilizzato al telescopio. Dopo aver costuito un OAM mode sorter per telescopi ottici, lo abbiamo testato all'osservatorio del Celado. I risultati ottenuti duranti una notte di osservazione mostrano che questo strumento potrebbe aprire la strada alla prima misurazione dell'OAM racchiuso nella luce proveniente da oggetti celesti.

Summary

Electromagnetic (EM) radiation carries energy and momentum.
Usually, associated to the momentum carried by light is the *linear momentum*, responsible for the radiation pressure and associated to a force action. Another component of the momentum is the *angular momentum*, which is associated to a torque action and which can be approximated under certain circumstances to the vectorial sum of the *spin angular momentum* and the *orbital angular momentum* (OAM). The spin angular momentum, the well-known component of the angular momentum, is associated to the right-handed or left-handed helicity of the light beam, therefore it is connected to the polarization. Recent studies gave evidence also to the importance of the orbital angular momentum of light. It is associated to a helicoidal shape of the wave front, caused by the precession of the Poynting vector around the propagation direction of the light beam. This new observable of the electromagnetic field finds several applications both in experimental and in theoretical physics and astrophysics, opening new scenarios to astronomy.
OAM finds practical use in many fields: radar, nanotechnology, quantum experiments, quantum information, etc. [25, 57]; in astronomy it is exploited to improve the resolving power of diffraction-limited optical instruments [77] and to facilitate the detection of extrasolar planets through the optical vortex coronograph [8, 24, 40, 41, 46, 49, 82]. Theoretical works show that it could be used as a new diagnostic instrument for the study of rotating gravitational fields, e.g. Kerr black holes [81], and that it could provide information about the spatial structure of the medium traversed by photons in their travel from the source to the observer [80].

In this thesis we study the propagation of orbital angular momentum of light for astrophysical applications and a possible method for OAM detection with optical telescopes. The main purpose of this work is to highlight that light can have a much more complex structure than what is usually thought by astronomers, and therefore can transport much more informa-

tion. In particular, this thesis deals with the orbital angular momentum of light as a new observable for astronomers, which could give additional information with respect to those already inferred from the analysis of the intensity, frequency and polarization of light.

In chapter 1 we introduce the concept of the orbital angular momentum of the electromagnetic radiation (and, in the quantum limit, of photons). Considering a beam of polarized laser light, it carries OAM when the electric field in cylindrical coordinates (r, θ, z) has the following form:

$$\vec{E}(\vec{r}, t) = \widehat{\sigma} u(r, \theta, z) e^{i(kz - wt)} + c.c.$$

where $\widehat{\sigma}$ is the polarization unit vector, *c.c.* represents the complex conjugate and the complex function $u(\vec{r}, \theta, z)$ is a function describing the form of the field amplitude profile, and is defined as:

$$u(r, \theta, z) = u_0(r, z) e^{i\ell\theta}.$$

We notice that the total phase of the field has acquired a new component, now we have:
$wave\ phase = kz - wt + \ell\theta$.
The component $\ell\theta$, where θ is an angle, is the azimuthal phase: it is because of the presence of this azimuthal component that the orbital angular momentum arises and the wave front acquires an helicoidal shape that wraps itself up around the propagation axis [3, 62]. The orbital contribution is determined solely by the azimuthal phase dependence and is equivalent to $\ell\hbar$ per photon. In a plane perpendicular to the propagation direction the phase undergoes ℓ times a change of 2π, and along the propagation axis a phase singularity appears, giving rise to an intensity pattern with the shape of a ring, because of destructive interference along the singularity.
A Laguerre-Gaussian beam, familiar from paraxial optics, is a physically realizable example of light with this phase distribution.

In chapter 2 we analyze the Anderson-Higgs mechanism of photon mass acquisition in a plasma and study the contribution to the mass from the orbital angular momentum acquired by a beam of photons when it crosses a spatially structured charge distribution. To this end we apply Proca equations in a static plasma with a particular spatial distribution of free charges, notably a plasma vortex, that is able to impose orbital angular momentum onto light. In addition to the mass acquisition of the conventional Anderson-Higgs mechanism, we find that the photon acquires an additional mass from the OAM and that this mass reduces the Proca photon mass. In this way we show that a photon acquires OAM every time it goes through a medium

with a density that is azimuthally inhomogeneous in the plane perpendicular to the propagation direction of the beam. Since this OAM depends on the spatial distribution of charges (in the plane perpendicular to the propagation direction), it could be exploited in astronomy to get information about the spatial structure of the traversed media. Thus, orbital angular momentum could be used by astronomers as a new diagnostic instrument: studying the OAM of light we catch with our astronomical telescopes could give us additional information about the density function of the interstellar medium traversed by photons.
The results of this chapter can be found in the publication "*Photon orbital angular momentum and mass in a plasma vortex*" [80].

In chapter 3 we report the results of real-world, outdoor radio experiments concerning the study of the propagation of orbital angular momentum: since OAM is a property of the electromagnetic field, it has the same behavior at all wavelengths. In these experiments we generated and propagated non-monochromatic incoherent radio waves with different OAM values to simultaneously transmit two radio channels on the same frequency encoded with different OAM states ($\ell = 0$ and $\ell = 1$). The positive outcome of this experiment shows that:

- non-monochromatic incoherent waves (which are interesting in the field of astronomy, since it is the main kind of light astronomers receive) preserve their orbital angular momentum signature in far-field;
- OAM states are orthogonal states, they do not influence each other, and their orthogonality is preserved.

From an astronomical point of view, this means that the message brought by light can arrive to us and we can aim at detecting it.
The results exposed in this chapter can be found in the publication "*Encoding many channels on the same frequency through radio vorticity: first experimental test*" [78].

If OAM can be a new astronomical observable carrying astrophysical information, and if this information is preserved during its propagation, next step is trying to measure OAM enclosed in light collected by astronomical telescopes. Up to now, OAM of light from astrophysical objects has never been detected. In chapter 4 we describe a possible way to detect OAM with optical telescopes through the so-called *OAM mode sorter* [15, 16, 43, 44], a device performing the OAM spectrum already used with laser light on optical benches, and that we have adapted to be used with optical telescopes. After having built an OAM mode sorter for optical telescopes, we tested it at Celado observatory. The results obtained during an observing

night show that this instrument could pave the way to the first detection of OAM of light from celestial objects.

Chapter 1

Orbital angular momentum of light

It has been recognized for a long time that a photon has spin angular momentum, observable macroscopically in a light beam as polarization. It is less well known that a beam may also carry orbital angular momentum linked to the wave phase structure. Although both forms of angular momentum have been identified in electromagnetic theory for very many years, it is only during the past decades that orbital angular momentum has been the subject of intense theoretical and experimental study.
The aim of this chapter is to give an overview on the orbital angular momentum of light.

1.1 Electromagnetic waves in classical physics

That light should have mechanical properties has been known, or at least suspected, since Kepler proposed that the tails of comets were due to the radiation pressure associated with light from the sun. A quantitative theory of such effects became possible only after the development of Maxwell's unified theory of electricity, magnetism and optics. However, his treatise on electromagnetism [52] contains only little about the mechanical effects of light. It was Poynting who quantified the momentum and energy flux associated with an electromagnetic field [67].

1.1.1 Maxwell's equations

In Maxwell's theory the electric field $\vec{E}(t,\vec{x})$ and the magnetic field $\vec{B}(t,\vec{x})$ are unified in a unique field, the electromagnetic field, which in empty space and in the presence of electric charges and conduction currents (respectively distributed with density $\rho(t,\vec{x})$ and $\vec{j}(t,\vec{x})$) is formally described by

Maxwell's equations:

$$\vec{\nabla}\cdot\vec{E} = \frac{\rho}{\varepsilon_0} \qquad \vec{\nabla}\times\vec{E} = -\frac{\partial\vec{B}}{\partial t} \tag{1.1}$$

$$\vec{\nabla}\cdot\vec{B} = 0 \qquad \vec{\nabla}\times\vec{B} = \mu_0\left(\vec{j}+\varepsilon_0\frac{\partial\vec{E}}{\partial t}\right) \tag{1.2}$$

where ε_0 is the electric constant (permittivity) in vacuum, μ_0 is the magnetic constant (permeability) in vacuum, $c = (\varepsilon_0\mu_0)^{-1/2}$ is the speed of light in vacuum, and we are using MKS system of units. From these fundamental equations we infer the following properties for an electromagnetic wave, traveling in a homogeneous and isotropic medium, with no free currents or free charges (empty to the limit):

1. $\vec{E}$ and $\vec{B}$ propagate with the same phase velocity v, which assumes the following value in vacuum:
   $v = c = 1/\sqrt{\varepsilon_0\mu_0} = 3\times10^8 m/s$;

2. the absolute values of the fields are connected by the proportionality relation:
   $B = E/v$, in vacuum $B = E/c$;

3. $\vec{E}$ and $\vec{B}$ are orthogonal to each other and to the direction of propagation: electromagnetic waves are transverse waves;

4. the direction of the vectorial product $\vec{E}\times\vec{B}$ defines the propagation direction, which is pointed by the wave vector $\vec{k}$.

Being vectorial properties of the field, these properties are valid in any coordinate system.

1.1.2 Electromagnetic potentials

Just as in mechanics, it turns out that in electrodynamics it is often more convenient to express the theory in terms of potentials rather than in terms of the electric and magnetic fields themselves.
Here I just give the definitions of the electromagnetic potentials, for any demonstration the reader can refer to chapter 3 of the book "*Electromagnetic Field Theory*" [85].

The electrostatic scalar potential

The time-independent electric (electrostatic) field $\vec{E}^{stat}(\vec{x})$ is irrotational, hence it may be expressed in terms of the gradient of a scalar field, that we denote by $-\phi^{stat}$:

$$\vec{E}^{stat}(\vec{x}) = -\vec{\nabla}\phi^{stat}(\vec{x}). \tag{1.3}$$

The magnetostatic vector potential

Since $\vec{\nabla} \cdot \vec{B}^{stat}(\vec{x}) = 0$ and any vector field $\vec{a}$ has the property that $\vec{\nabla} \cdot (\vec{\nabla} \times \vec{a}) \equiv 0$, we can always write:

$$\vec{B}^{stat}(\vec{x}) = \vec{\nabla} \times \vec{A}^{stat}(\vec{x}) \tag{1.4}$$

where $\vec{A}^{stat}(\vec{x})$ is called the *magnetostatic vector potential*.

The electrodynamic potentials

If we generalize the static analysis above to the electrodynamic case, *i.e.*, the case with temporal and spatial dependent sources $\rho(t, \vec{x})$ and $\vec{j}(t, \vec{x})$, we find the following expressions for the corresponding fields $\vec{E}(t, \vec{x})$ and $\vec{B}(t, \vec{x})$:

$$\vec{B}(t, \vec{x}) = \vec{\nabla} \times \vec{A}(t, \vec{x}) \tag{1.5}$$

$$\vec{E}(t, \vec{x}) = -\vec{\nabla}\phi(t, \vec{x}) - \frac{\partial}{\partial t}\vec{A}(t, \vec{x}) \tag{1.6}$$

where $\vec{A}(t, \vec{x})$ is the *electromagnetic vector potential*, and $-\vec{\nabla}\phi(t, \vec{x})$ is the *electromagnetic scalar potential*.

1.1.3 Energy and momentum of electromagnetic waves

Electromagnetic waves carry energy and momentum. The presence of an electric field $\vec{E}$ and a magnetic field $\vec{B}$ in a region of space involves the presence of a certain quantity of energy, distributed in that volume of space with density u; in a homogeneous medium the instantaneous electromagnetic energy density is

$$u = \frac{1}{2}\varepsilon E^2 + \frac{B^2}{2\mu} \tag{1.7}$$

where ε is the dielectric constant, and μ is the magnetic permeability of the medium.
It's useful to define the flux of electromagnetic energy traveling through a surface perpendicular to the direction of the wave propagation. This can be expressed by the electromagnetic energy flux or the Poynting vector, defined by:

$$\vec{S}_p = \frac{1}{\mu}\vec{E} \times \vec{B} \tag{1.8}$$

that can also be viewed as the electromagnetic energy current density. Its modulus expresses the electromagnetic energy per unit time that traverses the unit surface orthogonal to the propagation direction. Its direction is same of the wave vector $\vec{k}$.

The momentum carried by an electromagnetic wave in vacuum is expressed by the momentum density, or linear momentum density:

$$\vec{p} = \varepsilon_0 \vec{E} \times \vec{B} = \frac{\vec{S}_p}{c^2}. \tag{1.9}$$

1.2 The orbital angular momentum of light

1.2.1 OAM in classical electrodynamics

We start this section recalling how the orbital angular momentum of a system of massive particles is defined, in order to get to the definition of the orbital angular momentum of an electromagnetic wave by analogy. The orbital angular momentum density of a system of massive particles is given by:

$$\vec{j}^{mech}(\vec{x}) = \vec{x} \times \vec{p}^{mech}(\vec{x}) \tag{1.10}$$

where $\vec{x} = \vec{x}_r - \vec{x}_0$ is the radius vector connecting the reference system origin (in $\vec{x}_0$) with the point we are considering (in $\vec{x}_r$), and $\vec{p}^{mech}(\vec{x})$ is the linear momentum density in that point. The total angular momentum, which is given by the integral of $\vec{j}^{mech}$ over the volume V considered, can be decomposed into two parts:

$$\vec{J}^{mech} = \int_V \vec{j}^{mech}(\vec{x}) d^3x = \vec{L}^{mech} + \vec{S}^{mech} \tag{1.11}$$

where $\vec{L}^{mech}$ is the extrinsic angular momentum, that is the angular momentum associated to the motion of particles around the reference frame origin, whereas $\vec{S}^{mech}$ is the intrinsic angular momentum, that is the angular momentum describing the single particle rotation around itself. It is evident that the angular momentum of a body measured in its centre-of-mass reference frame is zero.
Now we go back to electromagnetic waves: the total angular momentum density in vacuum can be defined similarly to the previous case:

$$\vec{h} = \vec{x} \times \vec{p} = \varepsilon_0 \vec{x} \times [\vec{E} \times \vec{B}] \tag{1.12}$$

and the total angular momentum of the field in a volume V becomes

$$\vec{J} = \varepsilon_0 \int_V \vec{x} \times (\vec{E} \times \vec{B}) dx^3. \tag{1.13}$$

Careful examination of this last term shows that polarisation does not account for all of the angular momentum that can be carried by the electromagnetic field [75]. The part associated with polarisation is known as spin,

but in addition there is also an orbital contribution. Indeed, if we develop the previous expression, we obtain the result

$$\begin{aligned}\vec{J} = \varepsilon_0 \int_V \vec{E} \times \vec{A} d^3x + \varepsilon_0 \int_V \vec{x} \times [(\vec{\nabla}\vec{A}) \cdot \vec{E}] d^3x \\ - \varepsilon_0 \int_V \vec{\nabla} \cdot (\vec{E}\vec{x} \times \vec{A}) d^3x + \varepsilon_0 \int_V (\vec{x} \times \vec{A})(\vec{\nabla} \cdot \vec{E}) d^3x.\end{aligned} \tag{1.14}$$

If we:

- assume that the vector potential $\vec{A}$ is sufficiently well-behaved (it is regular enough and falls off sufficiently fast at large distances) that it can be Helmotz decomposed into a sum of an irrotational part, $\vec{A}^{irrot}$, and a rotational part, $\vec{A}^{rot}$, so that the magnetic field can always be expressed as $\vec{B} = \vec{\nabla} \times \vec{A}^{rot}$

- introduce the gauge invariant formula for the intrinsic part of the angular momentum, i.e. the part that is not dependent on the choice of the moment point $\vec{x}_0$,

$$\vec{S} = \varepsilon_0 \int_V \vec{E} \times \vec{A}^{rot} d^3x \tag{1.15}$$

  which we identify as the *spin angular momentum* (SAM)

- introduce the likewise gauge invariant extrinsic part, i.e. the part that does depend on the choice of $\vec{x}_0$,

$$\vec{L} = \varepsilon_0 \int_V \vec{x} \times [(\vec{\nabla}\vec{A}^{rot}) \cdot \vec{E}] d^3x + \int_V \vec{x} \times \rho \vec{A}^{rot} d^3x \tag{1.16}$$

  which we identify with the *orbital angular momentum* (OAM) (if there is no net electric charge density ρ, the second integral in the above expression vanishes)

after some calculations we find that expression (1.14) can be approximated as [85]:

$$\vec{J} = \vec{S} + \vec{L} - \varepsilon_0 \oint_\Sigma d^2x \hat{n} \cdot (\vec{E}\vec{x} \times \vec{A}^{rot}). \tag{1.17}$$

If $\vec{E}\vec{x} \times \vec{A}^{rot} \equiv \vec{E}(\vec{x} \times \vec{A}^{rot})$ falls off sufficiently fast with $\mid \vec{x} \mid$, the contribution from the surface integral $\oint_\Sigma$ in the previous expression can be neglected. This is the reason that why one usually considers the total angular momentum composed by two terms, the spin angular momentum, $\vec{S}$, and the orbital angular momentum $\vec{L}$:

$$\vec{J} = \vec{S} + \vec{L}. \tag{1.18}$$

With regard to the SAM, in 1909 Poynting reasoned that circularly polarised light must carry angular momentum [66], and in the 1930's Beth experimentally demonstrated his idea from the observation of the twisting moment (torque) which acted on a birefracting metal foil illuminated by circularly polarized light [20].
More recent is the discovery of the orbital angular momentum (OAM), which is connected with the spatial structure of the field [2]. If the SAM of light makes an absorbing particle spin around its own axis, the OAM of light makes the particle rotate around the beam axis ([4, 7, 32, 61, 73]).

1.2.2 OAM in quantum mechanics

In the previous section we have described the orbital angular momentum referred to a beam of light, whereas this section wants to be a brief summary about the characterization of the orbital angular momentum when referred to single photons.

Angular momentum operators

Quantum mechanics associates operators to the physical measurable quantities of a system (the observables): the possible and only result of a measurement is the average value of the operator associated to the quantity we are interested in, calculated with respect to the wave function describing the state of the system.
To the physical quantity *angular momentum*, quantum mechanics associates an operator $\widehat{J}$ [1] [13]. In the same way as for the classical field, this operator can be decomposed into two terms, corresponding to spin and orbital angular momentum [91]:

$$\widehat{J} = \widehat{S} + \widehat{L} \tag{1.19}$$

The z component of the orbital angular momentum operator turns out to be:

$$\widehat{L}_z = (\widehat{\vec{r}} \times \widehat{\vec{p}})_z = \frac{\hbar}{i}\left(\widehat{x}\frac{\partial}{\partial y} - \widehat{y}\frac{\partial}{\partial x}\right) = -i\hbar\frac{\partial}{\partial\theta} \tag{1.20}$$

which is valid in Cartesian and cylindrical coordinates respectively, where ϕ is the polar angle of $\vec{r}$.
The operators $\widehat{S}$, $\widehat{L}$ and $\widehat{J}$ satisfy the standard commutation rules for angular momentum operators:

$$[S_i, S_j] = \sum_k i\hbar\varepsilon_{ijk}S_k \tag{1.21}$$

[1] Differently from all the others sections, in this section the symbol ˆ indicates an operator instead of a unit vector.

$$[L_i, L_j] = \sum_k i\hbar\varepsilon_{ijk}L_k \tag{1.22}$$

$$[J_i, J_j] = \sum_k i\hbar\varepsilon_{ijk}J_k \tag{1.23}$$

for $i, j, k = x, y, z$, with ε_{ijk} the Levi-Civita pseudotensor.
Besides, in quantum regime there exists a severe limit on measurements of angular momentum: it is impossible to measure simultaneously the angular momentum and the spin of a photon

$$[\widehat{J}_i, \widehat{S}_j] = i\hbar\epsilon_{ijk}\widehat{S}_k, \tag{1.24}$$

the angular momentum and the orbital angular momentum

$$[\widehat{J}_i, \widehat{L}_j] = i\hbar\epsilon_{ijk}\widehat{L}_k, \tag{1.25}$$

and the spin and the orbital angular momentum

$$[\widehat{L}_i, \widehat{S}_j] = i\hbar\epsilon_{ijk}\widehat{S}_k. \tag{1.26}$$

This is expressed saying that the two operators associated to these physical quantities do not commute.

OAM quantization compared to spin quantization

The spin of the photon is connected to the helicity and is described by the circular polarization basis. The single photon spin along a fixed axis, e.g. z-axis, is:

$$S_z = s_z\hbar \tag{1.27}$$

where s_z can assume only two values: $s_z = \pm 1$. All the other values are possible only in beams of light, as superposition of the spin values of different photons. In light beams the spin angular momentum is connected to the polarization (figure 1.1):

$s_z = 0$ for linearly polarized waves,

$s_z = +1$ for waves with right circular polarization,

$s_z = -1$ for waves with left circular polarization,

$-1 < s_z < 1$ for elliptically polarized waves.

A deeper explanation of the concept of *spin* can be found in appendix A.

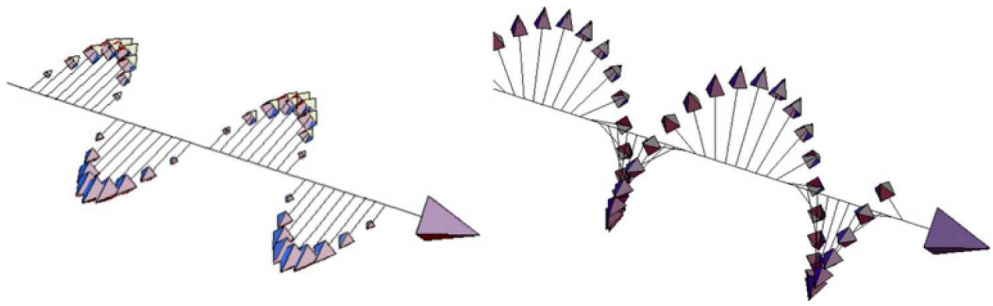

Figure 1.1: The spin angular momentum of light is connected to the polarization of the electric field. Left: light with linear polarization carries no spin. Right: right or left circularly polarized light carries a spin of $\pm\hbar$ per photon (source: A. M. Yao and M. J. Padgett, 2011 [94]).

On the other hand, the orbital angular momentum is described by the quantum number ℓ and at the single photon level its component along z-axis is:

$$L_z = \ell\hbar \tag{1.28}$$

where ℓ can assume any integer number, both positive and negative.

In classical electrodynamics it is connected with the spatial structure of the field and gives rise to a helicoidal form of the wave front (figure 1.2):

- if $\ell = 0$ the wave front is plane and the direction of the Poynting vector is the same of the wave vector direction, i.e. $\vec{S} \parallel \vec{k}$; [2]

- if $\ell \neq 0$ the wave front is helicoidal because, during the propagation of the electromagnetic wave (along the direction of $\vec{k}$), the Poynting vector spirals around $\vec{k}$, with constant inclination with respect to the propagation axis (see next section).

1.2.3 Intrinsic and extrinsic nature of OAM

For a light beam

When we study the motion of massive quanta, the spin angular momentum is considered as the intrinsic angular momentum, because it is the only angular momentum that remains constant when the reference frame chosen by the observer is changing. Instead, the orbital angular momentum of a

[2] When we mention the direction of the wave vector $\vec{k}$ we mean the *average* direction of the electromagnetic wave propagation. This direction does not always coincide with the *instantaneous* direction of propagation, which is represented instead by the Poynting vector direction $\vec{S}$.

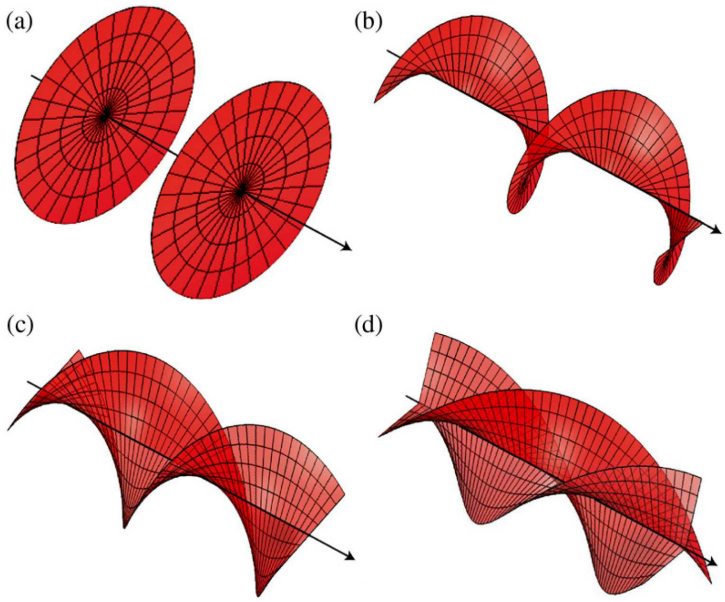

Figure 1.2: Plane wave front for (a) $\ell = 0$ and helical wave fronts for (b) $\ell = 1$, (c) $\ell = 2$ and (d) $\ell = 3$ (source: A. M. Yao and M. J. Padgett, 2011 [94]).

particle is considered extrinsic because its value depends on the reference frame chosen by the observer and it can even vanish when the observer is in the reference frame of the particle.
This distinction between spin and orbital angular momentum that applies to massive particles, is no more valid when we refer to paraxial beam of light. In this case, we have highlighted that spin is connected to the polarization, whereas the orbital angular momentum depends on the spatial structure of the beam, so it is possible to find even a paraxial beam of light with an intrinsic orbital angular momentum. We can find this situation when, in the reference frame we are considering, the transverse orbital angular momentum integrated over the entire plane perpendicular to the z axis of propagation is null. In other words, the spin angular momentum is always intrinsic, while the z component of the orbital angular momentum can be defined intrinsic only if the z direction is such that the transverse momentum integrated over the entire beam is null [58]. So, when we make sure the axis direction is chosen in order to obtain a null transverse momentum, we can state that the orbital angular momentum does not depend on which lateral position relative to the axis we select. Therefore, unlike the spin angular momentum of a light beam which is always intrinsic, the orbital angular momentum of an electromagnetic beam may be either extrinsic or intrinsic.

For a single photon

If we consider a single photon, its intrinsic properties are:

- null mass,

- null electrical charge,

- spin quantum number equal to 1.

These three properties define a photon, and do not depend on the chosen reference frame.
Orbital angular momentum is associated with the phase profile of the light beam and directly depends on the spatial coordinates: because of this, it is not an intrinsic property of photons, it is a property of the field. It can be defined for a single photon [45], but it depends on the reference frame used. Indeed, to define the OAM of a single photon, we need at least two photons (one used as a spatial reference for the other) or an axis to be used as a reference frame. So, we can define the OAM of a single photon, but this measurement requires an appropriate set-up of the experiment.
In [83], Tamburini and Vicino discussed that the OAM of a photon is an extrinsic property, i.e. OAM of a single photon depends on the used reference frame.

1.3 Paraxial beams of light: the Laguerre-Gaussian modes

In quantum mechanics the wave function describing a specific state of the analyzed system is represented by a vector in a space defined by a complete set of basic and arbitrary functions in a Hilbert space. The square of the absolute value of the components of such a vector along the axes of the adopted reference frame gives the probability to find our system in the states identified by the corresponding eigenvector axes. Analogously, the field amplitude of an electromagnetic wave can be described by using different orthonormal bases.
The modern study of optical angular momentum [25] can be said to have started with the paper of Allen et al. [2]. In this work it was found that Laguerre-Gaussian light beams possess an orbital angular momentum of $\ell\hbar$ per photon, where ℓ is the so-called azimuthal index of the beam. This paper showed that any beam with the following expression for the amplitude

distribution in cylindrical coordinates[3]:

$$u(r, \theta, z) = u_0(r, z)e^{i\ell\theta} \tag{1.29}$$

carried orbital angular momentum about the beam axis[4]. The orbital contribution is determined solely by the azimuthal phase dependence and is equivalent to $\ell\hbar$ per photon. A Laguerre-Gaussian beam, familiar from paraxial optics, is a physically realizable example of light with this phase distribution.

In the following sections, we are going to analyze light beams emitted by lasers under paraxial conditions (i.e., when the second order aberrations can be neglected), because under these conditions the separation of optical angular momentum into spin and orbital parts is straightforward. On the other hand, in exact (or non-paraxial) beams with $\exp(i\ell\theta)$ dependence, neither the spin nor the OAM are physically observable quantities. Indeed, in a general situation, the polarization and spatial degrees of freedom are coupled by Maxwell equations [9]. However, in beams with sizes much larger than the wavelength, which thus propagate in paraxial regime, both properties may be controlled separately.

Paraxial beams in a refractive medium

If the beam propagates paraxially in vacuum or in a homogeneous and isotropic medium, L_z and S_z are separately conserved. On the other hand, the anisotropy of a medium acts on the polarization and affects SAM, whereas the inhomogeneity of a medium acts on the wavefront and affects OAM [18][5].

1.3.1 Paraxial beams and nature of the orbital angular momentum

It is evident from equation (1.9) that the linear momentum of a plane wave lies along the direction of propagation (which we suppose to be along the z axis), so there cannot be any component of the angular momentum along

[3]If we consider a plane perpendicular to the propagation axis z, r is the distance from the propagation axis and θ is the azimuthal angle.

[4]In the literature, the argument of the exponential term can be expressed both with $+$ and with $-$ sign, it makes no difference for the discussion.

[5]Whenever SAM and OAM affect each other during propagation, optical *spin-orbit coupling* effects take place . A special case of spin-orbit coupling effect is *SAM-OAM conversion*, which is defined as an optical process in which SAM and OAM both vary during propagation but the total angular momentum is conserved, whatever the input state of light is [12, 50].

this direction. However, the electric and magnetic fields generated by a laser are not perfectly transverse, but they have some small components along direction $\widehat{z}$. Considering these beams of polarized laser light, the electric field in cylindrical coordinates (r, θ, z)[6] has the following form:

$$\vec{E}(\vec{r}, t) = \widehat{\sigma} u(r, \theta, z) e^{i(kz - \omega t)} + c.c. \tag{1.30}$$

where $\widehat{\sigma}$ is the polarization unit vector, ω is the angular frequency of the electromagnetic wave, *c.c.* represents the complex conjugate, and the complex function $u(r, \theta, z)$ is a function describing the form of the field amplitude profile, and is defined as:

$$u(r, \theta, z) = u_0(r, z) e^{i\ell\theta}. \tag{1.31}$$

We notice that the total phase of the field has acquired a new component, so now we have:
$wave\ phase = kz - \omega t + \ell\theta$.
The component $\ell\theta$, where θ is an angle, is the azimuthal phase: it is because of the presence of an azimuthal component of the linear momentum density that the orbital angular momentum arises [3]. In fact, in the case where the electric field and the magnetic field are transverse to the propagation direction $\vec{k}$, the linear momentum density $\vec{p} = \varepsilon_0 \vec{E} \times \vec{B}$ is parallel to $\vec{k}$ and therefore the integration of the angular momentum density (which varies according to the position with respect to the considered z axis, but which is always perpendicular to $\vec{k}$) turns out to be equal to zero. So, when the electromagnetic wave fields have no components along the propagation direction $\vec{z}$, there is no orbital angular momentum. Instead, when the electric field and the magnetic field of the electromagnetic wave have also a component along $\vec{k}$ [7], the linear momentum density is no more parallel to $\vec{k}$, therefore the radial and azimuthal components of $\vec{S}_p$ appear. This last component, in its turn, gives origin to an angular momentum density no more perpendicular to $\vec{k}$: in this way, when it is integrated, it does not completely cancel out, but a component along $\vec{k}$ remains still present. If those conditions are valid,

$$\vec{J} = \frac{1}{c^2} \int \vec{r} \times \vec{S}_p d\tau = \vec{J}_z \neq 0 \qquad \text{when } E_z \neq 0,\ B_z \neq 0, \tag{1.32}$$

then the Poynting vector $\vec{S}_p$ spins around the average propagation direction, and in this way it creates a helicoidal wave front and gives rise to the orbital angular momentum. It's important to put in evidence again that it is

[6] From now on it will be convenient the use of cylindrical coordinates (z, r, θ), with the z axis coinciding with the average direction of the field's propagation.

[7] In this $\vec{k}$case represents only the average propagation direction, but not the instantaneous one, i.e. the direction of the Poynting vector $\vec{S}_p$ is not constant.

fundamental the existence of the electric and the magnetic field components along $\vec{k}$: thanks to them the azimuthal and radial components of the linear momentum density are created, and when they are vectorially multiplied with $\vec{r}$, they generate a component of the angular momentum density along z, so that $\vec{J} = \vec{J}_z \neq 0$

We said that (1.31) is the complex scalar function describing the field amplitude distribution of a wave carrying OAM, and satisfying the wave equation in **paraxial approximation** conditions (i.e. $\mid \frac{\partial^2 \psi}{\partial z^2} \mid \ll k \mid \frac{\partial \psi}{\partial z} \mid$). In this approximation we do not consider the second derivative with respect to the z coordinate, so there are no second order aberrations. One can easily demonstrate that under these conditions the radial and azimuthal components along the z-axis of the linear momentum density $\vec{p} = \varepsilon_0 \vec{E} \times \vec{B}$ for a circular polarized beam propagating in the z direction are:

$$p_r = \varepsilon_0 \frac{\omega k r z}{z_R^2 + z^2} |u|^2, \tag{1.33}$$

$$p_\theta = \varepsilon_0 \left[\frac{\omega \ell}{r} |u|^2 - \frac{1}{2} \omega s_z \frac{\partial |u|^2}{\partial r} \right], \tag{1.34}$$

$$p_z = \varepsilon_0 \omega k |u|^2. \tag{1.35}$$

The component (1.33) is due to the divergence of the beam during its propagation. The first term of (1.34) depends on ℓ, where $\ell\hbar$ has been defined as the orbital angular momentum along z for the single photon; the second term is related to the spin, where $s_z\hbar$ is the spin angular momentum along z of the single photon. The last component, (1.35), is the linear momentum in the propagation direction.

In the description of the field given by Laguerre-Gaussian modes (an-

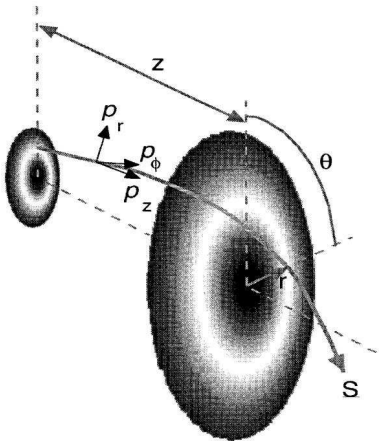

Figure 1.3: The trajectory of the Poynting vector and the components of linear momentum density (source: Allen et al. 1992 [2]).

alyzed in the next section), the temporal average of the real part of the linear momentum density of arbitrarily polarized light is given by:

$$\frac{\varepsilon_0}{2}(\vec{E}^* \times \vec{B} + \vec{E} \times \vec{B}^*) = i\omega\frac{\varepsilon_0}{2}(u^*\vec{\nabla}u - u\vec{\nabla}u^*) + \omega k\varepsilon_0|u|^2\widehat{z} + \omega s_z\frac{\varepsilon_0}{2}\frac{\partial|u|^2}{\partial r}\widehat{\theta} \tag{1.36}$$

where the first two terms are independent from polarization (one can demonstrate that the gradient is only on the azimuthal phase) and depend on the structure of the beam phase, while the last term depends on the polarization state and the gradient of the beam intensity [2]. So it is important to notice that:

- the orbital terms are generated by the phase gradient;

- the spin term is related to the polarization and the intensity gradient.

1.3.2 The Laguerre-Gaussian modes

The field amplitude of a laser light beam is well described by the Laguerre-Gaussian (LG) modes: in the paraxial approximation such modes satisfy Maxwell's equations [56] and represent the form of the amplitude profiles of the electric field inside a laser cavity [8]. Since the electric and magnetic fields in laser beams are not perfectly transverse, in Laguerre-Gaussian modes appears the term $exp(-i\ell\theta)$ which encodes an azimuthal phase and, consequently, an azimuthal angular momentum additional to spin angular momentum. These modes have a rotational symmetry along their own axis of propagation and an intrinsic orbital angular momentum $\ell\hbar$ for the single photon.
It is useful to express most beams in a complete basis set of orthogonal modes. For OAM carrying beams this is most usually the Laguerre-Gaussian mode set. Indeed, the analogy between quantum mechanics and optics in paraxial conditions[9] suggests that these modes are the autofunctions of the orbital angular momentum operator L_z. Thus, the Laguerre-Gaussian modes define a basis for the orbital angular momentum description in paraxial light beam, i.e. they constitute a complete set of orthonormal autofunctions, which are solutions of the paraxial wave equation.

[8] One can say the same for the Hermite-Gauss modes.

[9] There is a powerful analogy between paraxial optics and quantum mechanics. Here the Schrödinger wave equation is identical to the paraxial form of the wave equation with t replaced by z. The analogy allows much of paraxial optics, including orbital angular momentum, to be studied using the formalism of quantum mechanics.

A Laguerre-Gaussian mode has amplitude:

$$u_{pl}(r,\theta,z) = \frac{C}{(1+z^2/z_R^2)^{1/2}} \left[\frac{r\sqrt{2}}{w(z)}\right]^{\ell} L_p^l \left[\frac{2r^2}{w^2(z)}\right] \exp\left[\frac{-r^2}{w^2(z)}\right] \exp\left[\frac{-ikr^2 z}{2(z^2+z_R^2)}\right] \times \\ \times \exp(-i\ell\theta) \exp\left[i(2p+\ell+1)\tan^{-1}\left(\frac{z}{z_R}\right)\right] \tag{1.37}$$

where z_R is the Rayleigh range, $w(z)$ is the beam waist, L_p^ℓ is the associated Laguerre polynomial, and C is the constant of normalization. The integers p and ℓ are indices characterizing the different Laguerre-Gaussian modes:

- the index ℓ represents the number of helices interweaving each other within the space of a wavelength λ and is equal to the OAM parameter ℓ; when Laguerre-Guassian modes are interfered with a plane wave, we observe on a screen ℓ spiral arms (fig. 1.4);

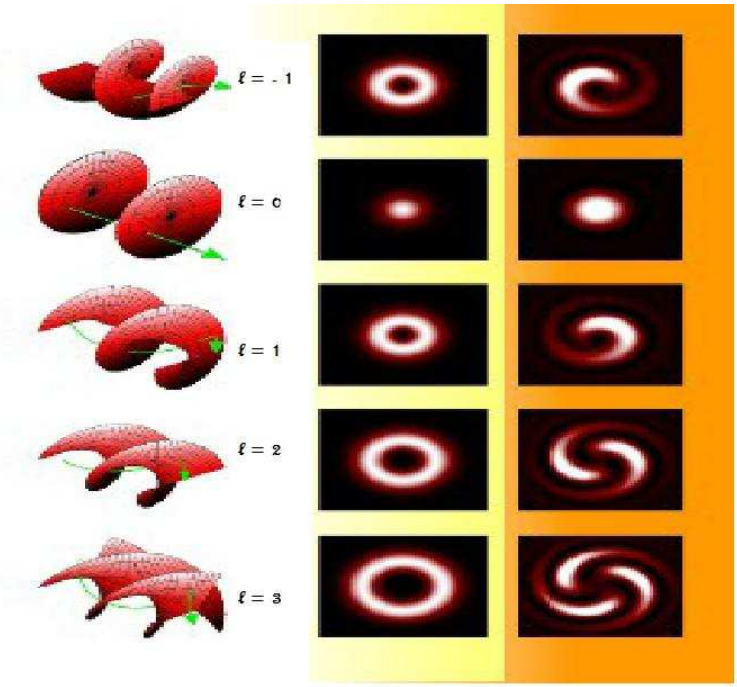

Figure 1.4: On the left: wave front shapes for different ℓ values. In the middle: LG intensity patterns on a plane perpendicular to the propagation direction. On the right: intensity patterns on a plane perpendicular to the propagation direction for Laguerre-Gaussian beams interfered with a plane wave. $p = 0$ for each beam. (source: Optics Group of the University of Glasgow, www.physics.gla.ac.uk/Optics/Miles).

- the index p constitutes the number of radial nodes; $(p+1)$ is the number of rings we see on a screen when we observe a Laguerre-Gaussian beam (fig. 1.5).

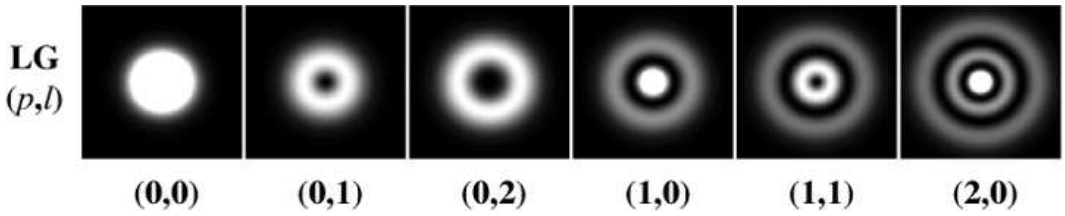

Figure 1.5: Laguerre-Gaussian intensity patterns, for different ℓ and p values (source: Sasada Lab., Department of Physics, Keio University, http://www.phys.keio.ac.jp/guidance/labs/sasada/research/orbangmom-en.html).

When $\ell = 0$ and $p = 0$ Laguerre-Gaussian modes reduce to Gaussian modes (i.e. modes where the function describing the spatial distribution of the field in the plane perpendicular to the propagation direction is a Gaussian function) because the beam has no orbital angular momentum.
Instead, for a Laguerre-Gaussian mode with $\ell \neq 0$, surfaces of constant phase have helicoidal form and the resulting phase discontinuity (the singularity) which is present along the axis, causes the annulment of the intensity along the axis.

1.3.3 The Poynting vector in Laguerre-Gaussian modes

If we neglect small terms in the $\widehat{z}$ coefficient, the Poynting vector for a Laguerre-Gaussian mode with linear polarization becomes [62]:

$$\vec{S}_p = C\frac{z_r}{z_r^2 + z^2}\left(\frac{zr}{z_r^2 + z^2}\widehat{r} + \frac{\ell}{kr}\widehat{\theta} + \widehat{z}\right) \tag{1.38}$$

where z is the distance from the beam waist, z_r is the Rayleigh range, k is the wave number, and C is a constant which depends on the radial position within the intensity distribution, the wavelength of the light and is proportional to the total power in the beam. The presence of the component $\widehat{\theta}$ implicates that the Poynting vector has an azimuthal component during its propagation: therefore it spirals around the propagation axis, as we can see in figure 1.6.
Let us summarize: the intensity pattern projected by a LG beam on a screen perpendicular to the propagation direction has the following characteristcs:

- if $\ell = 0$
    - for $p = 0$: Laguerre-Gaussian modes reduce to Gaussian modes, the beam has no orbital angular momentum. The Poynting vector is parallel to the z axis, giving rise to a spot of light with intensity decreasing from the spot's center to outside, according to a typical gaussian profile;

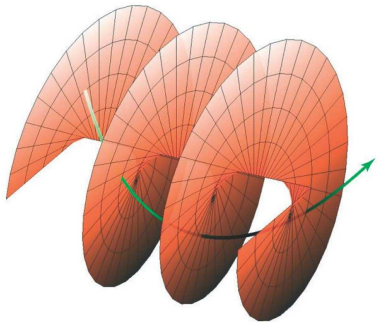

Figure 1.6: The helical wavefront characterized by an azimuthal phase term ($\ell = 1$) and the associated Poynting vector, the azimuthal component of which gives rise to an orbital angular momentum (source: Torres et al. 2011 [88])

  - for $p \neq 0$: a central spot of light is still present, and around it there are p concentric rings;

- if $\ell \neq 0$: the Poynting vector, spinning around the z axis, creates a field distribution with $(p + 1)$ maxima, which originate $(p + 1)$ concentric rings around a singularity with null intensity. The radius of the rings is proportional to the ℓ value.

From equation (1.38) we find that, away from the beam waist, the azimuthal rotational velocity is given by:

$$\frac{\partial \theta}{\partial z} = \frac{\ell}{kr} z^2. \tag{1.39}$$

From this equation we see that, fixing constant the radius, the Poynting vector follows a spiral path, characterized by a constant angle between $\vec{S}_p$ and $\vec{k}$, given by

$$\theta = \frac{\ell}{kr} \tag{1.40}$$

and by a step z_p necessary to carry out a complete rotation of 360°, expressed as:

$$z_p = \frac{2\pi k r^2}{\ell}. \tag{1.41}$$

We notice that $z_p \propto r^2$, so in the proximity of the z axis the Poynting vector spirals around $\vec{k}$ with a short step, whereas moving away from the axis of the beam we find that $\vec{S}_p$ spirals with a step greater and greater, infinite to the limit (see figure 1.7).

1.4 Optical vortices

Traditionally wave propagation is analyzed by means of regular solutions of wave equation. These solutions often have some singularities, namely some

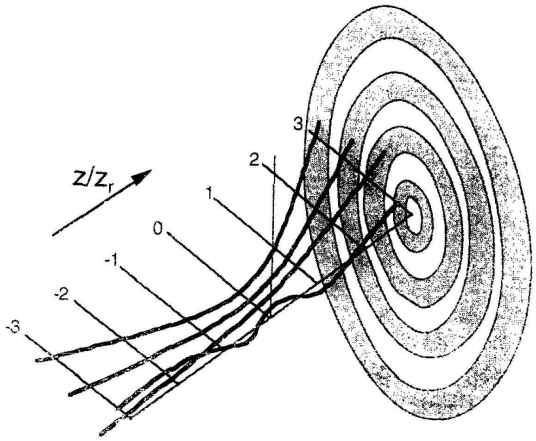

Figure 1.7: Propagation of the Poyinting vector associated to the different rings of the Laguerre-Gaussiam mode $p = 3$, $\ell = 1$ (source: Allen et al. 1995 [62]).

points or lines in the space where the mathematical quantities describing the physical properties of waves become infinite or change abruptly. For example, a phase singularity is a point where the wave phase is undefined and intensity vanishes. Phase singularities can be found in every type of wave, from tidal waves whose singularity is the point at which all cotidal lines meet and at which tide height vanishes giving rise to a whirlpool, to electromagnetic waves.
In waves of light, phase singularities [19, 21] form the so-called *optical vortices*. Phase singularities are topological features of the wave front, which one can find in light beams having orbital angular momentum: indeed, the helicoidal form of wave front causes an indetermination of phase on the axis around which the wave front wraps itself up. This wave front discontinuity along the axis has a null field intensity associated, due to the destructive interference of all the different wave phases which meet along the axis [47]. In other words, the phase of an electromagnetic wave carrying a certain quantity of orbital angular momentum turns out to be undefined along the propagation axis, because it is where different wave phases join, giving rise to destructive interference. Therefore such phase singularities of the wave function appear as points where the wave function modulus becomes equal to zero, and are called *dislocations* or *optical vortices*: such a name is due to the structure of the surface of constant phase, which looks like a dislocation with the form of a helix, and to the direction of the phase gradient, which spins and wraps itself up around the singularity line, similarly to a fluid in a water whirlpool. The Poynting vector spins around the vortex nucleus in a given direction: from equation (1.39) we infer that at the centre of the vortex this rotational velocity is infinite. So, the features of an optical vortex are essentially two (fig. 1.8):

1. a wave front with a helicoidal form, therefore the beam of light is endowed with orbital angular momentum,

2. a wave front discontinuity along the propagation direction, therefore a phase discontinuity: light intensity is equal to zero along that axis (no more gaussian spot of light, but rings of light around a singularity with null intensity).

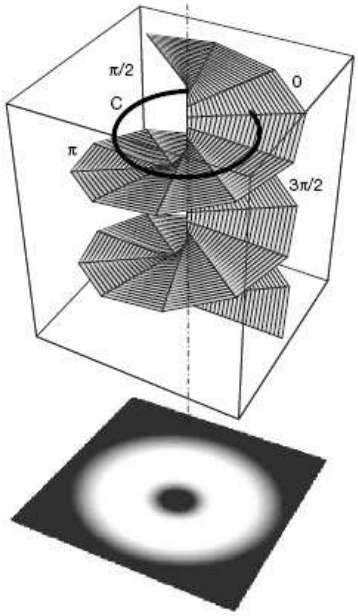

Figure 1.8: The wave front (top) and the intensity pattern (bottom) of the simplest Laguerre-Gaussian mode. The index ℓ is referred to as the winding number, and $(p+1)$ is the number of radial nodes. Here we only consider the case of $p = 0$. The azimuthal phase term $\exp(i\ell\theta)$ of the Laguerre-Gaussian modes results in helical wave fronts. The phase variation along a closed path C around the beam center is $2\pi\ell$. Therefore, in order to fulfill the wave equation, the intensity has to vanish in the center of the beam (source: Mair et al. 2001 [47]).

Phase singularities (or *dislocations*, or *optical vortices*) are characterized by the fact that phase undergoes a changing of an entire multiple of 2π along a closed circuit C around the middle of the vortex (fig. 1.9). As a consequence, it becomes useful to define the concept of topological charge of an optical vortex. We remind that, in order to describe the field amplitude, we have defined a complex scalar function given by eq. (1.31), which can be expressed also in the following way:

$$u(\vec{r}) = |u(\vec{r})|e^{i\chi(\vec{r})} \tag{1.42}$$

where $\chi(\vec{r})$ represents the phase of the wave amplitude.

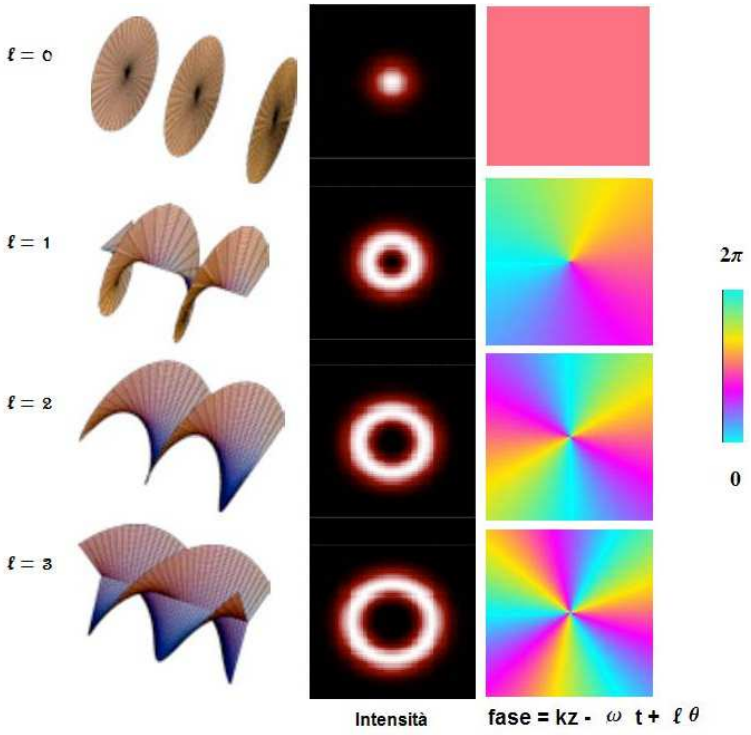

Figure 1.9: On the left: wave front shapes for different ℓ values and $p = 0$. In the middle: LG intensity patterns on a plane perpendicular to the propagation direction. On the right: phase variation on a plane perpendicular to the propagation axis, with different colours for different phase values (source: Optics Group of the University of Glasgow, www.physics.gla.ac.uk/Optics/Miles).

The topological charge of the vortex is defined as the circuitation of the phase gradient around the singularity, so we define the topological charge as the following integral:

$$Q = \frac{1}{2\pi} \oint_c \nabla\chi \cdot d\vec{s} \tag{1.43}$$

which is positive if the phase grows up along the path of integration, and negative in the opposite case. It is evident that it turns out to be:

$$Q = \ell, \tag{1.44}$$

so the topological charge of the vortex is a measure of the orbital angular momentum of the beam [42].
The phase variation along the closed path C circuiting the centre of the beam is $2\pi\ell$, therefore intensity must vanish in the middle of the beam in order to fulfill the wave equation. The value of ℓ is the number of times the phase undergoes a change of 2π in a wavelength, whereas its sign represents the handedness of OAM.

Optical vortices in Nature

Optical vortices do not represent a purely artificial feature of light (originated, for example, when a beam of laser light goes through a hologram created by computers, or a spiral phase plate [11, 89]), but can be generated naturally by some deformations of the wave front, which can be caused by the passing through a non linear medium.
Anisotropic optical vortices occur in speckle patterns, which arise naturally from the interference of a large number of more or less random plane waves [17]. At particular places in a speckle pattern the amplitude of the field vanishes, causing the phase to be singular. Around these phase singularities an optical vortex is formed, whose exact form is determined by the local interference of plane waves. Natural optical vortices are anisotropic, i.e. they still have a complex amplitude with an azimuthal behaviour characterized by the term $\exp(i\ell\theta)$ but, unlike isotropic optical vortices, the phase increase does not go linear with the azimuth coordinate θ. Not only does the phase increase in a nonlinear way around an anisotropic vortex, also the intensity profile around it is anisotropic, i.e. the lines of constant intensity are ellipses (fig. 1.10).
Describing the azimuthal behaviour of the field around an anisotropic op-

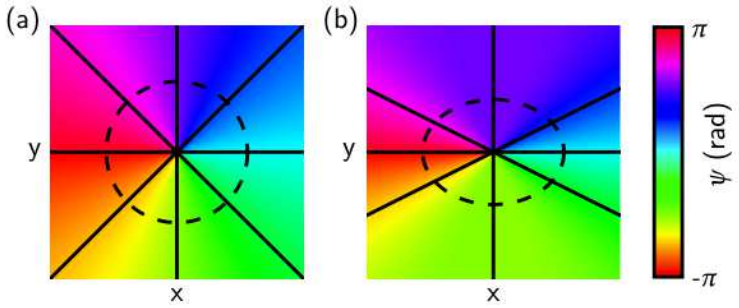

Figure 1.10: Phase of the field for (a) an isotropic $\ell = 1$ optical vortex and (b) an anisotropic $\ell = 1$ optical vortex. Black lines (there are eight lines, from the center outwards) indicate equal-phase lines and are spaced $\pi/4$ radians apart. In (b) the lines are more closely spaced around the y axis, showing the anisotropic character of the vortex. In addition, the dashed lines indicate lines of constant intensity. For an isotropic optical vortex, the lines of constant intensity are circles, while for an anisotropic optical vortex they are ellipses (source: Berkhout 2011 [17]).

tical vortex requires more than one pure optical vortex mode, such that the field can be decomposed in the orthogonal basis of pure vortex modes:

$$u(\theta) = \sum_{\ell} \frac{c_\ell}{\sqrt{2\pi}} e^{i\ell\theta} \tag{1.45}$$

where the factor $1/\sqrt{2\pi}$ ensures the normalization. The coefficient c_0 is related to the local intensity of the field, the coefficients c_{-1} and c_{+1} are related to the derivatives of the field. In the case of an isotropic optical vortex $c_\ell = \delta_{\ell,m}$, where $\delta_{i,j}$ is the Kronecker delta.

The optical vortex coronograph

Light coming from astronomical sources can be manipulated at the telescope. We have seen that when a beam of light carries orbital angular momentum, its intensity vanishes on the propagation axis: this property of optical vortices can be used in astronomical field to detect extrasolar planets. Using appropriate manipulation of light, one can induce orbital angular momentum in the light coming from the on-axis star, in order to obscure it and allow to observe nearby planets, which otherwise would be invisible because of the great difference of their magnitude with respect to the star. In this case star light behaves like a coronograph for itself [8, 24, 40, 41, 46, 49, 82].

Chapter 2

Photon orbital angular momentum and mass in a plasma vortex

As astronomers, we are interested in how the orbital angular momentum of light can be exploited in the field of astronomy:

- astronomers may *produce* OAM:
  - with the so-called *optical vortex coronograph*, an optical instrument that exploits the geometrical properties of optical vortices to allow seeing very faint objects near very bright objects, that would normally be obscured by glare (e.g. extrasolar planets near their host star). Vortices are artificially produced by optical elements (spiral phase plates) inserted in the optical path of light through the telescope, so that the light of the on-axis source (e.g. the hosting star) is rejected without altering the light of off-axis sources (e.g. extrasolar planets) [8, 24, 40, 41, 46, 49, 82];
  - to overcome the Rayleigh criterion limit with optical vortices, in order to resolve two sources at angular distances much below the Rayleigh limit [77];
- astronomers may *use OAM as a new diagnostic observable of light*, in order to get additional information about the Universe [23, 31], in particular about:
  - very massive and rotating objects, e.g. Kerr black holes, since their space-time dragging can imprint OAM on light passing through their surroundings [81];
  - inhomogeneous plasmas traversed by photons during their travel from the astrophysical source to the observer (this is the topic dealt with in this chapter) [80].

In this chapter we analyze the mechanism of photon mass acquisition in a plasma and study the contribution to the mass from the orbital angular momentum acquired by a beam of photons when it crosses a spatially structured charge distribution. To this end we apply Proca-Maxwell equations in a static plasma with a particular spatial distribution of free charges, notably a plasma vortex, that is able to impose OAM onto light. In addition to the mass acquisition of the conventional Anderson-Higgs mechanism, we find that the photon acquires an additional mass from the OAM and that this mass reduces the Proca photon mass.
The results exposed in this chapter can be found in the publication "*Photon orbital angular momentum and mass in a plasma vortex*" [80].

2.1 Introduction

Influenced by results derived in 1962 by Schwinger [71], in 1963 Anderson showed that a photon propagating in a plasma acquires a mass, called also *effective mass*, defined as:

$$m_{eff} = \frac{\hbar\omega_p}{c^2} \tag{2.1}$$

where ω_p is the plasma frequency[1], $\hbar$ is the reduced Planck constant and c is the velocity of light in vacuum [5, 54]. In this process the photon acquires an effective mass because of its interaction with plasmons (collective oscillations of the free electron gas density at precise frequencies) [53].
In order to study photons that have acquired an effective mass, it is convenient to replace Maxwell's equations by Proca-Maxwell equations, which are the equations describing a massive electromagnetic field [29, 37]. In this chapter we are going to use this approach to analyze the contribution to the mass from the orbital angular momentum acquired by a beam of photons as it traverses a spatially structured charge distribution.
OAM can be generated by the imprinting of vorticity onto the phase distribution of a beam when it crosses inhomogeneous non-linear optical systems [6] or particular spatial structures such as fork holograms or spiral phase plates. Such a beam can be described by a superposition of Laguerre-Gaussian (LG) modes characterized by the two integer-valued indices ℓ and p [2]. The azimuthal index ℓ describes the number of twists of the helical wavefront in a wavelength and the radial index p gives the number of radial nodes of the mode. The electromagnetic field amplitude of a generic LG

[1]Free electrons and positive ions within a plasma have densities oscillating at a natural frequency ω_p, the *plasma frequency*. It defines a cutoff frequency below which there is no electromagnetic propagation and the penetrating wave drops off exponentially, while at frequencies above ω_p absorption is small and the plasma is transparent.

mode, in a plane perpendicular to the direction of propagation, is

$$F_{pl}(r,\theta) = \sqrt{\frac{(\ell+p)!}{4\pi p!}} \left(\frac{r^2}{w^2}\right)^{|\ell|} L_p^{|\ell|}\left(\frac{r^2}{w^2}\right) e^{-\frac{r^2}{2w^2}} e^{i\ell\theta} \tag{2.2}$$

obeying to the orthogonality condition

$$\int_0^\infty r dr \int_0^{2\pi} F^*_{p\ell} F_{p'\ell'} d\theta = \delta_{pp'}\delta^{\ell\ell'} \tag{2.3}$$

where w is the beam waist, $L_p^{|\ell|}$ is the associated Laguerre polynomial, and r and θ are the cylindrical coordinates in the plane perpendicular to the direction of propagation z. As we stated in chapter 1, the phase factor $\exp(-i\ell\theta)$ is associated with an OAM of $\ell\hbar$ per photon, and a phase singularity is embedded in the wavefront, along the propagation axis, with a topological charge ℓ [2, 93].

As is well known, not only the linear momentum of light but also its angular momentum can propagate to infinity [38, 72, 85]. The OAM property of the field remains stable during the propagation in free space and has been experimentally verified down to single-photon limit [58]. It has also been studied theoretically [83].

Different is the case of photons propagating in inhomogeneous media [39]. The exchange of angular momentum between a photon beam and a plasma vortex and the possible excitation of photon angular momentum states in a plasma was analyzed in ref. [55]. In this chapter we show that the OAM acquired by a photon in a spatially structured plasma can be interpreted as an additional mass-like term that appears in Proca equations. More specifically, we study the propagation of a photon with wavelength λ in a static helicoidally distributed plasma with step $q_0 = \lambda/b$, where b is an integer.

The possibility of studying space plasma vorticity remotely by measuring the OAM of radio beams interacting with the vortical plasma was pointed out by Thidé in 2007 [84]. Here we analyze this possibility theoretically by studying the exchange of angular momentum between a plasma medium and a photon beam.

2.2 Photons in a static plasma vortex

Let us consider an isotropic plasma, cast to form a helicoidal static plasma vortex. The heavy ions constitute a neutralising background and their motion can, in the first approximation, be neglected. If we consider transverse electromagnetic waves propagating through this kind of plasma, we can

describe them by the electric field propagation equation[2]

$$\left(\nabla^2 - \frac{1}{v_{ph}^2}\frac{\partial^2}{\partial t^2}\right)\vec{E} = \mu\frac{\partial\vec{j}}{\partial t} \tag{2.4}$$

where $v_{ph} = (\varepsilon\mu)^{-1/2}$ is the phase velocity of light in a medium with permittivity ε and permeability μ, and the electron current $\vec{j} = -en\vec{v}$ is determined by the electron fluid equations

$$\frac{\partial n}{\partial t} + \nabla \cdot n\vec{v} = 0, \tag{2.5}$$

$$\frac{\partial\vec{v}}{\partial t} + \vec{v}\cdot\nabla\vec{v} = -\frac{e}{m}(\vec{E} + \vec{v}\times\vec{B}). \tag{2.6}$$

where n is the electron number density, $\vec{v}$ is the velocity of the electrons in the medium, e is the electron electric charge and m is the electron mass. Thermal and relativistic mass effects are ignored.
The presence of a static plasma perturbation with helical structure brings about a new definition of the mean electron velocity and density, which become:

$$\vec{v} = \vec{v}_0(\vec{r}, t) + \delta\vec{v} \tag{2.7}$$

where $\vec{v}_0$ is the background velocity and $\delta\vec{v}$ is the perturbation associated with the propagating electromagnetic wave, and

$$n = n_0 + \tilde{n}(r, z)\cos(\ell_0\theta + q_0 z) \tag{2.8}$$

where n_0 is the background plasma density, and the plasma helix vortex density perturbation is described by the second term. It is expressed in cylindrical coordinates, $\vec{r} \equiv (r, \theta, z)$, and it depends on the distance with respect to the vortex axis of symmetry and can vary slowly along z, on a scale much longer than the spatial period $z_0 = 2\pi/q_0$ (where q_0 is the helix step)[3] .
So, ignoring the plasma rotation and considering the case of a static helical perturbation, the current density of the plasma now becomes $\vec{j} = -en(\vec{r})\delta\vec{v}$, and the propagation equation of the electric field takes the following form:

$$\left\{\nabla^2 - \frac{1}{v_{ph}^2}\frac{\partial^2}{\partial t^2} - \frac{\omega_{p0}^2}{v_{ph}^2}[1 + \varepsilon(r, \theta, z)]\right\}\vec{E} = 0 \tag{2.9}$$

where

$$\omega_{p0}^2 = \frac{e^2 n_0}{\varepsilon_0 m} \tag{2.10}$$

[2]We use MKS system of units.
[3]For a typical double vortex we will have $\ell_0 = 1$.

represents the square of the frequency of the plasma with no density perturbation (where ε_0 is the permittivity of free space), and

$$\varepsilon(r,\theta,z) = \frac{\tilde{n}(r,z)}{n_0}\cos(\ell_0\theta + q_0 z) \tag{2.11}$$

expresses the vortex perturbation.
We further assume that waves propagate along the vortex axis Oz, and consider solutions of the form

$$\vec{E}(\vec{r},t) = \vec{A}(\vec{r})\exp\left[-i\omega t + i\int^z k(z')dz'\right] \tag{2.12}$$

where ω is the wave frequency, $k = 2\pi/\lambda$ is the wave number, and $\vec{A}(\vec{r})$ is the wave amplitude: it varies slowly along z and satisfies [4]

$$\left|\frac{\partial^2\vec{A}}{\partial z^2}\right| << \left|2k\frac{\partial\vec{A}}{\partial z}\right|. \tag{2.13}$$

We can reduce the wave equation (2.9) to the perturbed paraxial equation:

$$\left[\nabla_\perp^2 + 2ik\frac{\partial}{\partial z} - \frac{\omega_{p0}^2}{v_{ph}^2}\varepsilon(r,\theta,z)\right]\vec{A} = 0 \tag{2.14}$$

with the dispersion relation connecting k and ω that has the form:

$$k^2 = \frac{1}{v_{ph}^2}(\omega^2 - \omega_{p0}^2). \tag{2.15}$$

We observe that if there was no vortex perturbation, equation (2.14) would reduce to the usual paraxial optical equation [5]. Instead, considering our case characterized by a vortex perturbation, a general solution to the wave equation in the paraxial approximation can be represented in a basis of orthogonal Laguerre-Gaussian modes, according to the expansion [55]

$$\vec{A}(r,\theta,z) = \sum_{p\ell} A_{p\ell}(r,z)e^{i\ell\theta}e^{-\frac{r^2}{2w^2}}\hat{e}_{p\ell} \tag{2.16}$$

where $w \equiv w(z)$ is the beam waist, $\hat{e}_{p\ell}$ are unit polarization vectors and $A_{p\ell}$ are the amplitudes, defined by

$$A_{p\ell}(r,z) = A_{p\ell}(z)\sqrt{\frac{(\ell+p)!}{4\pi p!}}\left(\frac{r^2}{w^2}\right)^{|\ell|}L_p^{|\ell|}\left(\frac{r^2}{w^2}\right) \tag{2.17}$$

[4] Equation (2.13) states that an acceleration (the term on the left) is much smaller than the corresponding velocity (the term on the right), and so it mathematically expresses that $\vec{A}(\vec{r})$ varies slowly along z.

[5] The paraxial equation is the equation describing the wave in the immediate vicinity of the optical axis.

where $L_p^{|\ell|}(x)$ are the associated Laguerre polynomials, the integer p is the radial quantum number and ℓ is the azimuthal quantum number. Substituting equation (2.16) in equation (2.12), we can express the total electric field as a superposition of Laguerre-Gaussian states:

$$\vec{E}(\vec{r},t) = \sum_{p\ell} \vec{E}_{p\ell}(\vec{r}) \exp\left(-i\omega t + i\int^z k(z')dz'\right) \tag{2.18}$$

with

$$\vec{E}_{p\ell}(\vec{r}) = \vec{A}_{p\ell}(z) F_{p\ell}(r,\theta) \tag{2.19}$$

where $F_{p\ell}(r,\theta)$ is the one given in eq. (2.2). When a vortex perturbation $\varepsilon(r,\theta,z)$ is present, these modes will be coupled to each other through the relation [55]

$$\frac{\partial}{\partial z} A_{p\ell}(z) = \frac{i}{2kv_{ph}^2} \sum_{p'\ell'} K(p\ell, p'\ell') A_{p'\ell'} \tag{2.20}$$

where $K(p\ell, p'\ell')$ are the coupling coefficients, defined by:

$$K(p\ell, p'\ell') = \omega_{p0}^2 \int_0^\infty r dr \int_0^{2\pi} F_{p\ell}^* F_{p'\ell'} \varepsilon(r,\theta) d\theta. \tag{2.21}$$

They can be reduced to

$$K(p\ell, p'\ell') = \omega_{p0}^2 \delta_{pp'} \int_0^{2\pi} \varepsilon(\theta) e^{i(\ell'-\ell)\theta} d\theta \tag{2.22}$$

when we consider the simplest case, that is the case when ε depends only on the azimuthal angle θ [6].
Let's try to understand the physical meaning of the mode coupling. We have to imagine that the photon, traveling through the static plasma vortex, bumps into the electrons forming the vortex, and the different and subsequent impacts generate the photon orbital angular momentum. Obviously, there is not a transfer of a sharp OAM characterized by a precise topological charge l, but as long as the photon goes through the plasma, it hits electrons and, by this way, acquires orbital angular momentum.

Generally speaking, it is important to highlight that the superposition of states is different from the coupling. In fact, in superposition the different states are independent, while in coupling the different states depend on each other, according to a defined relation. So, in coupling, a mode is not necessarily composed by all the other modes. An example is given by the case analyzed right now: the mode coupling is weak, and so it is simply given by a basic mode and some perturbations.

[6] This expression remains valid when the radial scale of the plasma vortex is much larger than the photon beam waist $w(z)$.

Special solution: photon beam with no initial OAM

Now we want to analyze the special case of:

- a photon beam with no initial OAM, and that can be described by $\vec{E}_{pl} = 0$ for $l \neq 0$. We are particularly interested in this case because ordinary stars should not emit OAM, so starlight traversing interstellar plasma should have no initial orbital angular momentum;

- a mode coupling sufficiently weak to consider the zero OAM mode dominant over the entire interaction region, such that $|E_{p0}| >> |E_{p'l'\neq 0}|$. We are interested in this assumption because it reflects the characteristics of rarefied astrophysical plasmas.

So, starting from a helical static plasma perturbation defined by equation (2.9), with these assumptions we obtain [55]:

$$K(pl, p'l') = \pi\omega_{p0}^2 \frac{\tilde{n}}{n_0} \delta_{pp'} [\delta_{l',-l_0} e^{iq_0 z} + \delta_{l',l_0} e^{-iq_0 z}] \tag{2.23}$$

Now we substitute this expression of the coupling coefficients in the coupled mode equation (2.20), then we integrate over the axial coordinate z and finally we obtain $A_{pl}(0) = A(0)\delta_{l0}$. If we assume the same polarization state for all the interacting modes, we find that the field mode amplitudes are given by

$$A_{p,\pm l_0}(z) = i\frac{\pi A(0)}{2c^2} \int_0^z \frac{\omega_{p0}^2(z')}{k(z')} \frac{\tilde{n}(z')}{n_0} e^{\mp iq_0 z'} dz'. \tag{2.24}$$

The rate of transfer of OAM from the static plasma vortex to the electromagnetic field is described by this equation. We have to notice that this last equation is only valid when the transfer of OAM is small, such that the amplitude of the initial Gaussian mode A_{p0} can be considered constant along the axis.

General solution: photon beam with an initial OAM

A more general solution, where the amplitude of the initially excited mode is allowed to change, is discussed in ref. [55]. The authors show that the initial OAM state ℓ_i of the electromagnetic beam passing through the vortex plasma decays over all the other states $(\ell_i + u\ell_0)$, where u is an integer, on a length scale approximately determined by the inverse of the coupling constant, showing an effective exchange of OAM states between photons and plasma.

2.3 Proca equations

When one considers a photon propagating in a plasma, the usual Maxwell's equations can be replaced by the set of Proca equations (or Maxwell-Proca equatios) in which there appears a mass-like term for the photon due to light-matter interaction [37].
In the presence of charges ρ and currents $\overrightarrow{j}$, the three-dimensional version of the Proca equations, can be written in terms of the electric $\vec{E}$ and magnetic $\vec{B}$ fields (in SI units) as:

$$\nabla \cdot \overrightarrow{E} = \frac{\rho}{\varepsilon_0} - \mu_\gamma^2 \phi \tag{2.25}$$

$$\nabla \times \overrightarrow{E} = -\frac{\partial \overrightarrow{B}}{\partial t} \tag{2.26}$$

$$\nabla \cdot \overrightarrow{B} = 0 \tag{2.27}$$

$$\nabla \times \overrightarrow{B} = \mu_0 j + \mu_0 \varepsilon_0 \frac{\partial \overrightarrow{E}}{\partial t} - \mu_\gamma^2 \overrightarrow{A} \tag{2.28}$$

(where ε_0 and μ_0 are the permittivity and the permeability of free space respectively) together with the equations

$$\vec{B} = \nabla \times \vec{A} \tag{2.29}$$

$$\vec{E} = -\frac{\partial \vec{A}}{\partial t} - \nabla \phi \tag{2.30}$$

and the Lorentz condition

$$\nabla \cdot \overrightarrow{A} = -\frac{1}{c^2} \frac{\partial \phi}{\partial t} \tag{2.31}$$

where $\overrightarrow{A}$ is the vector potential, $c = (\varepsilon_0 \mu_0)^{-1/2}$ is the phase velocity of light in vacuum, and ϕ is the scalar potential. μ_γ^{-1} is a characteristic length associated with the photon rest mass m_γ by the relation:

$$m_\gamma = \frac{\mu_\gamma \hbar}{c} \tag{2.32}$$

For m_γ tending to zero, Proca equations smoothly reduce to Maxwell's equations.
The Poynting vector for massive photons depends directly on both the scalar and the vector potentials

$$\overrightarrow{S} = \frac{1}{\mu_0} (\overrightarrow{E} \times \overrightarrow{B} + \mu_\gamma^2 \phi \overrightarrow{A}) \tag{2.33}$$

and also the energy density of the massive electromagnetic field has an explicit dependency on the potentials

$$u = \frac{1}{2} (\varepsilon_0 \overrightarrow{E}^2 + \frac{1}{\mu_0} \overrightarrow{B}^2 + \varepsilon_0 \mu_\gamma^2 \phi^2 + \frac{1}{\mu_0} \mu_\gamma^2 \overrightarrow{A}^2). \tag{2.34}$$

2.3.1 Proca equations for photons in a plasma

We have seen that a photon in a plasma gains an effective mass. On the other hand we have seen Proca equations, which are equations describing massive photons. Therefore we can try to use Proca equations to describe the motion of photons in a plasma.
Before starting our analysis, it is important to remark that the scalar potential ϕ appearing in Proca equations and in the expression of the Poynting vector and of the energy density u for a massive electromagnetic field must be set equal to zero. In fact we know that along a fixed direction, e.g. the z direction, the photon has spin with only two values, ± 1, the third component $S_z = 0$ does not have meaning because it is not a property of the photon. So the photon rest mass has to be null because, according to Heitler, if the photon had a finite rest mass, three independent polarizations would exist, including a longitudinal polarization [35]. In a plasma there is not an effective longitudinal component of polarization, because the one we find actually is given simply by the scattering processes with electrons, and not by a a real intrinsic nature of the photon. Therefore the lack of this third spin component induces to consider equal to zero the photon rest mass. As a consequence ϕ must be null, because such a scalar field is also massive.

If we want to apply Proca equations to the plasma case, we have to insert the effective photon mass that a photon acquires going through a plasma. The photon mass in Proca equations is expressed by equation

$$m_\gamma = \frac{\mu_\gamma \hbar}{c} \tag{2.35}$$

whereas the effective photon mass is

$$m_{eff} = \frac{\omega_p \hbar}{c} \tag{2.36}$$

so, comparing these two equations, the inverse of the characteristic length in a plasma, μ_γ, is equal to the plasma frequency: $\mu_\gamma = \omega_p$.
With these assumptions ($\phi = 0$ and $\mu_\gamma = \omega_p$) the equations describing a massive electromagnetic field become:

$$\nabla \cdot \overrightarrow{E} = \frac{\rho}{\varepsilon_0} \tag{2.37}$$

$$\nabla \times \overrightarrow{E} = -\frac{\partial \overrightarrow{B}}{\partial t} \tag{2.38}$$

$$\nabla \cdot \overrightarrow{B} = 0 \tag{2.39}$$

$$\nabla \times \overrightarrow{B} = \mu_0 J + \mu_0 \varepsilon_0 \frac{\partial \overrightarrow{E}}{\partial t} - \omega_p^2 \overrightarrow{A}, \tag{2.40}$$

the Poynting vector takes the form

$$\overrightarrow{S} = \frac{1}{\mu_0}(\overrightarrow{E} \times \overrightarrow{B}) \tag{2.41}$$

and the energy density is expressed by:

$$u = \frac{1}{2}\left(\varepsilon_0 \overrightarrow{E}^2 + \frac{1}{\mu_0}\overrightarrow{B}^2 + \frac{1}{\mu_0}\omega_p^2 \overrightarrow{A}^2\right). \tag{2.42}$$

Let's start to develop the four-dimensional expression of Proca equations in the case of a plasma. When considering the electromagnetic wave equation of the Proca field, one obtains a Klein-Gordon equation for the 4-vector potential A_μ:

$$(\Box - \mu_\gamma^2) A_\mu = -\mu_0 j_\mu \tag{2.43}$$

where $\Box = (\frac{\partial^2}{\partial t^2} - \nabla^2)$ is the D'Alembertian differential operator. By differentiating this expression with respect to time, and considering the simplest case where μ_γ is a constant in time, one obtains

$$(\Box - \mu_\gamma^2)\frac{\partial}{\partial t} A_\mu = -\mu_0 \frac{\partial}{\partial t} j_\mu \tag{2.44}$$

This last equation is constituted by four components, and separating the temporal component from the spatial one we have:

$$\begin{cases} (\Box - \mu_\gamma^2)\frac{\partial}{\partial t} A_0 = \mu_0 \frac{\partial}{\partial t}\rho \\ \\ (\Box - \mu_\gamma^2)\frac{\partial}{\partial t} A_i = \mu_0 \frac{\partial}{\partial t} j_i. \end{cases} \tag{2.45}$$

From now on we are interested only in the second equation of (2.45). We want to apply these equations to the case of photons moving in a plasma, in particular we consider the case of a plasma with a well-defined structure, a static plasma vortex. In this case the current density has the form $\vec{j} = -en(\vec{r})\delta\vec{v}$, so its derivative becomes

$$\frac{\partial}{\partial t} j_i = -e[\delta\vec{v}\frac{\partial}{\partial t} n(\vec{r}) + n(\vec{r})\frac{\partial}{\partial t}\delta\vec{v}] = -en(\vec{r})\frac{\partial}{\partial t}\delta\vec{v} \tag{2.46}$$

where the first term in the square brackets has been eliminated because we are considering a *static* plasma vortex, so the density $n = n(\vec{r})$ is not a function of time. Since we are considering the case of a rarefied plasma (because it is the case of interstellar plasmas), $v_{ph} \sim c$ and from now on we use the unitary value for the phase velocity of light in vacuum, i.e.

$v_{ph} \sim c = 1$. Thus, from the second equation in (2.45) and from equation (2.46), in the case of a static plasma vortex one finds

$$(\Box - \mu_\gamma^2)\frac{\partial}{\partial t}\vec{A} = -en(\vec{r})\frac{\partial}{\partial t}\delta\vec{v}. \tag{2.47}$$

Using equation (2.30) ($\vec{E} = -\nabla\phi - \partial\vec{A}/\partial t$) and remembering that we are considering a scalar potential ϕ equal to zero, we can substitute the vector potential so that the last equation can be expressed as

$$(\Box - \mu_\gamma^2)\vec{E} = en(\vec{r})\frac{\partial}{\partial t}\delta\vec{v}. \tag{2.48}$$

Explicating the D'Alembertian, assuming that $\delta\vec{v}$ is parallel to $\vec{E}$ (remember that $\delta\vec{v}$ is the perturbation of electrons velocity associated with the propagating electromagnetic wave), and substituting from now on the light velocity in vacuum (which, in our case, is a good approximation of the phase velocity of light in the plasma, v_{ph}) with the unitary value, $c = 1$, we can write

$$\left(\frac{\partial^2}{\partial t^2} - \nabla^2 - \mu_\gamma^2 - \frac{en(\vec{r})\partial_t\vec{v}}{\varepsilon_0|\vec{E}|}\right)\vec{E} = 0. \tag{2.49}$$

We want to compare this last equation (which is an expression of the Proca equations applied to a rarefied plasma, so that $v_{ph} \sim c$, with a static vortex density) to the equation derived by the electric field propagation equation developed for the case of a static plasma vortex, which was:

$$\left\{\nabla^2 - \frac{\partial^2}{\partial t^2} - \omega_{p0}^2[1 + \varepsilon(r, \varphi, z)]\right\}\vec{E} = 0. \tag{2.50}$$

In order to make equal these last two equations, (2.49) and (2.50), we arrive at the following relation:

$$\mu_\gamma^2 + \frac{en(\vec{r})}{\varepsilon_0|\vec{E}|} = \omega_{p0}^2[1 + \varepsilon(r, \varphi, z)] \tag{2.51}$$

where, as we stated previously, ε_0 is the permittivity constant of the vacuum, while ε expresses the vortex perturbation. Explicating the ω_{p0} and ε terms (defined by equations (2.10),(2.11)) we obtain

$$\mu_\gamma^2 = \frac{e^2 n_0}{\varepsilon_0 m} + \frac{e^2}{\varepsilon_0 m}\tilde{n}\cos(l_0\varphi + q_0 z) - \frac{en(r)}{\varepsilon_0|\vec{E}|} \tag{2.52}$$

which after some passages can be written as:

$$\mu_\gamma^2 = \frac{e}{\varepsilon_0}\left(\frac{e}{m} - \frac{1}{|\vec{E}|}\right)[n_0 - \tilde{n}\cos(l_0\varphi + q_0 z)]. \tag{2.53}$$

This is the key equation, which shows that there is a relation between the effective mass that a photon acquires in a plasma and the orbital angular momentum. In fact, if we remember that:

- μ_γ is related to the photon effective mass gained in a plasma,
- $\tilde{n}(r,z)\cos(l_0\varphi + q_0 z)$ is related to the vortex perturbation, which in section (2.2) we showed to cause a transfer of OAM to the electromagnetic field traversing it

we understand the meaning of equation (2.53):

1- the negative term in the effective photon mass acquired in a turbulent plasma can be interpreted as an expression of orbital angular momentum. It can be considered as a fictitious term, because it is an interaction term generated by the scattering of photons with electrons in a plasma, and cannot be ascribed as an intrinsic property of the photon;

2- when the electron number density exhibits certain spatial properties, such as vortices, any photon has an associated virtual mass term that is smaller than that expected from Proca equations in a homogeneous plasma, because of a negative term that corresponds to a precise orbital angular momentum component.

So every time a photon goes through a plasma, it gains this virtual mass term that corresponds to a precise orbital angular momentum component, if the density of electrons has certain spatial properties. The electron number density does not necessary need to exhibit a vortex structure, what is necessary is that it is azimuthally inhomogeneous in the plane perpendicular to the propagation's direction of the electromagnetic beam.

From an ideal to the real case of OAM transfer

If we want to study the orbital angular momentum gained by a photon passing through a real plasma, we have to consider the special case of a static plasma vortex, even if we will never find a plasma with such a precise well-defined spatial distribution. We are interested in understanding this particular case, because it can be used as a basis to build any other type of structure. The real problem is extremely complex and difficult to resolve, so we can analyze the simplest special solution, and consider our problem as a superposition of many simple solutions, whose combinations could give every possible value of orbital angular momentum.

For example, a simple planar slab of astrophysical plasma with uniform electron spatial density can be represented by the superposition of left-handed and right-handed plasma vortices that gives a final null OAM component as expected.

2.4 Conclusions

In this chapter we have investigated the problem of photon mass in an inhomogeneous plasma and showed that part of the acquired mass term is related to the orbital angular momentum of light imposed by certain spatial distributions of plasma electrons. We have focused our attention on the simplest case of spatial distribution described by a static plasma vortex. This approach shows that the spatial distribution of charges can impose OAM, and that this OAM is related to an additional mass term that reduces the effective mass of the photon inside a non-structured plasma. When the density function of the traversed plasma is azimuthally inhomogeneous in the plane perpendicular to the propagation's direction of the electromagnetic beam, we have found that the virtual photon mass term is smaller than that expected from Proca equations in a homogeneous plasma, because of a negative term that corresponds to a precise orbital angular momentum component. In this case, a cascading process of OAM transfer between the plasma and the photon beam is achieved, which is related to the electron number density function.
Therefore, studying the OAM of light we collect with our telescopes could give additional information about the spatial structure of the interstellar medium traversed by photons during their travel from the source to the observer. OAM of light could acquire the same importance as spectroscopy: spectroscopy can give us information about the energy of light, while the orbital angular momentum could provide us information about the spatial structure of the traversed media.

Chapter 3

Experimental verification of vorticity preservation in the far field

In the previous chapter we have shown that the orbital angular momentum encoded in a beam of light can bring further information about the universe, in particular about the spatial structure of the traversed media [80]. We also know that orbital angular momentum can be imparted by the space-time dragging of massive rotating sources, so it can bring information about these kind of objects, in particular Kerr black holes [81].
Therefore, if orbital angular momentum can be seen as an additional carrier of information, now it is important to test if its topology (which is connected to the orbital angular momentum value) is preserved in the far field. This chapter deals with an outdoor test we performed, which for astronomical purposes has the meaning of an experimental confirmation of a theoretical prediction, first made almost a century ago by Abraham [1], that the total electromagnetic angular momentum can propagate over huge distances. This test was done in the radio domain: since OAM is a property of the electromagnetic field, it has the same behaviour at all wavelengths.
We have shown experimentally how to propagate and use the properties of twisted non-monochromatic incoherent radio waves to simultaneously transmit two radio channels on the same frequency encoded with different orbital angular momentum states. The positive outcome of this experiment shows that:

- non-monochromatic incoherent waves (which are interesting in the field of astronomy, since they are the main kind of light astronomers collect with their instruments) preserve their orbital angular momentum signature in far field;

- OAM states are orthogonal states, they do not influence each other, and their orthogonality is preserved.

Apart from the field of astronomy, in the radio domain the natural consequence of these properties is a novel radio technique, which allows the implementation of, in principle, an infinite number of channels in a given, fixed bandwidth, even without using polarization, multiport or dense coding techniques.
The results exposed in this chapter can be found in the publication "*Encoding many channels on the same frequency through radio vorticity: first experimental test*" [78].

3.1 Introduction

Here we report the results of real-world, outdoor radio experiments in the 2.4 GHz band (it's the same band than WiFi). The results reported here show that OAM and vorticity are preserved throughout the long-distance propagation. Therefore, from an astronomical point of view, i.e. when we are the receivers of electromagnetic radiation, this means that the message brought by light can arrive to us [1]; from a telecommunications point of view, when we are also the transmitters, this means that OAM states can be used as a new and very large set of communication channels that are mutually orthogonal to each other in the OAM state space [86].
Our findings extend previous indoor laboratory test experiments in which the transmission of optical OAM states [28] and radio [79] beams was demonstrated.

3.2 Our apparatus: technical details

In our radio vorticity communication experiments, we generated and detected two orthogonal OAM channels within a fixed frequency band: one untwisted with OAM $\ell = 0$ and the other with an $\ell = 1$ OAM twist. Two identical WiFi FM transmitters, each with an output power of 2 Watt and driven by a signal generator, were tuned to the carrier frequency of 2.414 GHz to feed two antennae. In an FM transmission the amplitude and intensity of the electromagnetic wave remain constant in time, only the carrier frequency is modulated. The signal-to-noise ratio of the WiFi modules was 39 dB for the video channel and 45 dB for the audio band. The receiver sensitivity was -90 dBm [2] , i.e. 10^{-9} mW. The transmitted signal bandwidths of both signals were 15 or 27 MHz (like those used in video signals).

[1] Obviously, for frequency domains affected by the terrestrial atmosphere, this is true when we can neglect or compensate for or remove the effects of the turbulent atmosphere on the wave phase.

[2] The *decibel* (dB) is a logarithmic unit that indicates the ratio of a physical quantity (usually power or intensity) relative to a specified or implied reference level. A ratio in

The $\ell = 0$ source was radiated with linear polarization by a commercial 16.5 dBi gain Yagi-Uda antenna.
To generate the $\ell = 1$ vortex beam, we mechanically modified a pair of 26 dBi commercial off-axis steel parabolic antennas [3], with 15° offset and diameter $D = 80$ cm, to attain an off-axis spiral parabolic-shaped phase mask reflector. To get the parabolic shape the dish was transformed into a vortex reflector by attacching together the two antennas, one upon the other, and elevating, from the original shape, the surface of the antenna laying on the top (see fig. 3.1). The elevation, H, depends on the desired ℓ value, and is related to the wavelength λ by the following relation:

$$\ell = \frac{\Delta n \cdot H}{\lambda} \tag{3.2}$$

where Δn is the difference between the refractive index of the medium before the wave impinges on the antenna, and the one after. Since in our case we have a reflection, $\Delta n = 2$. Thus, if our wavelength is $\lambda \sim 12.5$ cm, and if we want $\ell = 1$, H has to be ~ 6.25 cm.

The expected beam waist, given by the diffraction limit of the antenna, is $\Delta\varphi = 1.22\lambda/D \approx 10.9°$. The half-power beam width (HPBW), i.e. the angular separation between the points on the antenna radiation pattern at which the power or, equivalently, the linear momentum, drops to half its maximum value is $\theta = k\lambda/D = 8.75°$, where k is the characteristic parameter of the antenna [4]. The $\ell = 1$ beam was also linearly polarized.
Additional technical details of the experiment and some definitions of antenna parameters can be found in the last section of this chapter and in appendix B.

---

decibels is ten times the logarithm to base 10 of the ratio of two quantities. For example, the ratio of a power value P_1 to another power value P_2 can be represented by the ratio expressed in decibels, L_{dB}, which is:

$$L_{dB} = 10 \log_{10} \left(\frac{P_1}{P_2} \right). \tag{3.1}$$

dBm, i.e. dB(mW), is the power relative to 1 milliwatt.
dBi, i.e. dB(isotropic), is the forward gain of an antenna compared with the hypothetical isotropic antenna, which uniformly distributes energy in all directions (linear polarization of the electromagnetic field is assumed unless noted otherwise).

[3] Parabolic antennas can be classified by the type of feed, that is, how the radio waves are supplied to the antenna. For an off-axis or offset feed parabolic antenna, the reflector is an asymmetrical segment of a paraboloid, so the focus, and the feed antenna, are located to one side of the dish. The purpose of this design is to move the feed structure out of the beam path, so it does not block the beam.

[4] The characteristic parameter of the antenna is a factor that depends on the shape of the reflector and the method of illumination.

Figure 3.1: The helicoidal parabolic antenna.

3.3 Intensity mapping of the twisted field

As a fist step, we experimentally characterized the physical properties of the twisted uncorrelated[5] non-monochromatic[6] EM wave train, proving that vorticity (and therefore OAM) can indeed be radiated into the far zone (in principle all the way to infinity [85]) and that the topological properties of twisted waves, namely the presence of the singularity and the spatial phase signature, are preserved in the far field zone.
For an antenna, the Fraunhofer or Rayleigh distance d_R at which the near/far field transition zone exists, is determined by the largest dimension of the antenna, D, and the operating wavelength λ, by the following relationship:

$$d_R = 2\frac{D^2}{\lambda}. \tag{3.3}$$

In our case with $D = 80$ cm and $\lambda = 12.5$ cm, it turns out to be 10.24 m. The intensity distribution of the radio vortex was mapped out 40 m (320λ) distant from the transmitting antenna. The HPBW diameter of the twisted parabolic antenna at 40 m distance is of the order of 6 m. The radio noise background measured in a 15 MHz bandwidth centered on the carrier frequency $\nu = 2.414$ GHz was -90 dBm. The polarization of the signal was linear and kept fixed horizontally. For safety reasons a calibrated 10dB signal attenuator was inserted at the output of the transmission line. As shown in figure 3.2, we determined the position of the field singularity with

[5]The EM wave train is uncorrelated because it is composed by two independent beams, $\ell = 0$ and $\ell = 1$.

[6]The EM wave train is non-monochromatic because it is frequency-modulated (FM transmission).

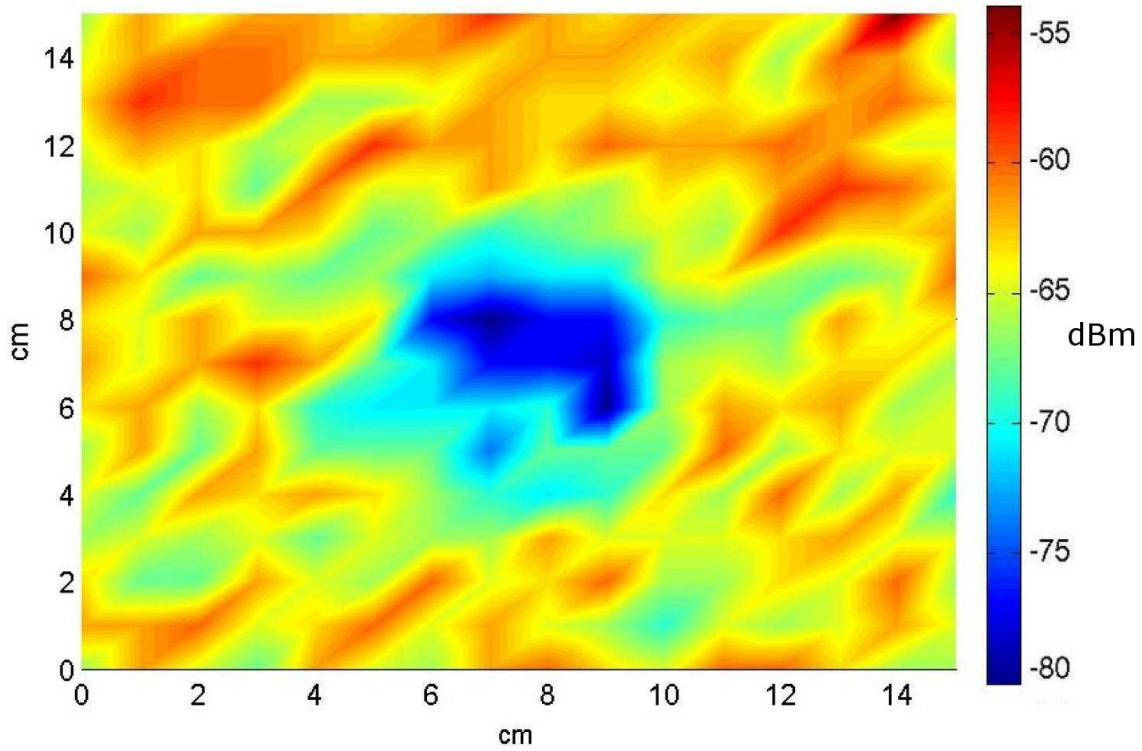

Figure 3.2: Intensity map of the radio beam vortex at 40 m (320λ) in free space in the region around the singularity. The intensity distribution in this regions exhibits fluctuations caused by environmental interference effects and perturbations. The central dip indicates the region where the field singularity is located, less than 3 cm wide, with a measured intensity of -82 dBm. The actual position of the singularity was confirmed by the phase change measured by the two-antenna interferometer (see text). The electromagnetic background is -90 dBm. The scale is in centimeters.

an inaccuracy of 3 cm ($\sim 0.24\lambda$). This inaccuracy was due to the experimental limitations dictated by the resolving power of the spectrum analyser used for sampling the electric field. The average intensity measured in the 3 cm region around the singularity was -82 dBm.

That the minimum found was the phase singularity of the field was confirmed by measuring the phase distribution around it with a phase interferometer: it was constructed from two identical Yagi-Uda antennae deployed along a baseline perpendicular to the direction of the transmitter, as can be seen in figure 3.3. Firstly we positioned the centre of the interferometer's baseline where the minimum of the field was measured and then we mechanically tilted the transmitting antenna in the horizontal and vertical directions and measured the ensuing phase change.

Finally, we verified the phase and field intensity distribution of the Yagi-Uda antenna used for transmitting the untwisted signal during the following experiment in Venice. No appreciable phase twist in the Yagi-Uda beam

was detected.

Figure 3.3: The phase interferometer constructed from two identical Yagi-Uda antennae positioned along a baseline perpendicular to the direction of the transmitter (the helicoidal parabolic antenna is in the background, on the top left corner of the picture). The two antennae are connected together with a 180°-phase-shifted cable through a beam adder module, in order to obtain a phase-difference interferometer. They can be mechanically tilted in the horizontal and vertical directions. The center of the interferometer's baseline was positioned where the minimum of the field was measured.

3.4 Radio transmission with orbital angular momentum

The purpose of the second stage of the experiment was to transmit with the same antennas, on the same frequency of 2.414 GHz, and within a fixed given bandwidth, two mutually orthogonal OAM modes, $\ell = 0$ and $\ell = 1$ at a distance of 442 meters (3536λ) from the phase-detecting interferometer. After having verified that the phase properties of the twisted beam were preserved, by analyzing the beam shape with an intensity/spectrum analyzer, we transmitted the two OAM modes from the lighthouse of San Giorgio Island (the transmitters can be seen in figure 3.5) in the direction

of the balcony of Palazzo Ducale in Venice (Italy), where they were received (figure 3.4). The HPBW diameter of the parabolic antenna at that distance was 67 meters. During the experiment, we measured a maximum signal power $P_{max} = 30.7$ dBm, with a background noise of -87 dBm generated by external radio sources.

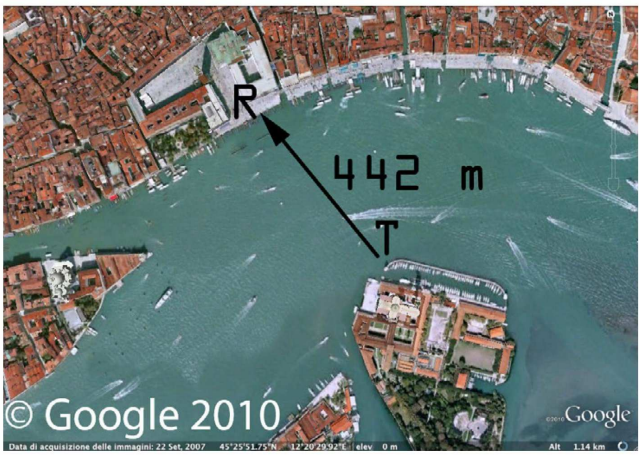

Figure 3.4: View of the San Marco experiment site in Venice, Italy (reproduced from Google Earth). The T and R letters indicate the locations of the transmitters and receivers respectively.

At the phase singularity point, we expected the field to drop almost to zero, as found in experiments at optical frequencies. The narrow zone where the central singularity was located, defined by a 10 dB (i.e. tenfold) drop in the mean field intensity, had a diameter of about 2λ. This small region was contained inside a wider zone with a diameter of $\sim$ 190 cm ($\sim 15\lambda$) where a 3-5 dB drop in the mean field intensity was observed. Outside this region, at distances larger than 2 m ($\sim 16\lambda$) from the singularity, the field intensity was found to be more stable and flatter. The measured signal intensity was only 3 dB lower than expected from a non-helicoidal parabolic antenna with the same diameter. The field strength, measured around the beam singularity, was higher than expected from a perfectly coherent beam. In fact, the signal intensity near the singularity, where the electric field is expected to tend to zero, exhibited a more uniform and flatter intensity profile than expected from a coherent beam with a Laguerre-Gaussian profile. The phase distribution of the entire antenna lobe was preserved. This actually resembles the behaviour typical of incoherent beams carrying OAM. Such beams preserve the phase profile but the region of the lobe in which the singularity is located appears much more filled by the signal because of the large width of the transmission band and, in our case, probably also because of the shape of the transmitting antenna. The only insignificant

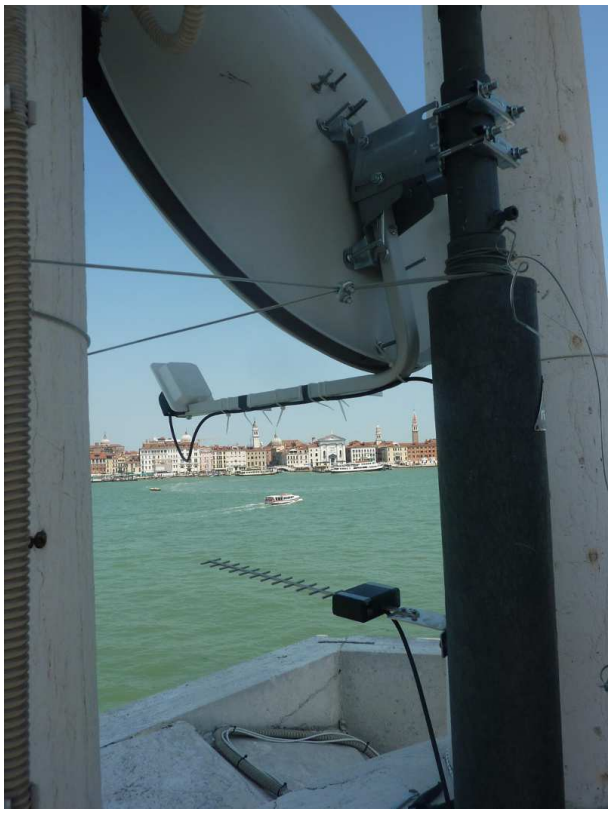

Figure 3.5: The two transmitters located in the lighthouse of San Giorgio island (in front of Palazzo Ducale, at a distance of 442 m). The helicoidal parabolic antenna generates the $\ell = 1$ signal, while the Yagi-Uda antenna below transmits the $\ell = 0$ signal.

variable interference noted during the experiments was due to reflections of the beam from the water surface of the lagoon that varied with the tidal height of the sea.
By using an interferometric phase discrimination method we were able to separate the two OAM modes by identifying their "phase fingerprints" [64, 79] . The receiving station consisted of a COTS (commercial off the shelf) frequency-modulation (FM) radio module receiver fed by two identical 16.5 dBi Yagi-Uda antennas (hereafter called antenna A and antenna B) connected together with a 180°-phase-shifted cable through a beam adder module, in order to obtain a phase-difference interferometer (figure 3.6). We decided to use such directive antennas to spatially reduce any possible background interference due to the presence of other WiFi sources. The antenna parameters are given in the appendix at the end of this chapter. Antenna A was mounted on a mechanical translator oriented towards the direction of the transmitting station to select one of the two channels by exploiting the spatial phase front properties of different OAM states present in the two beams, whereas antenna B could be moved mechanically in the

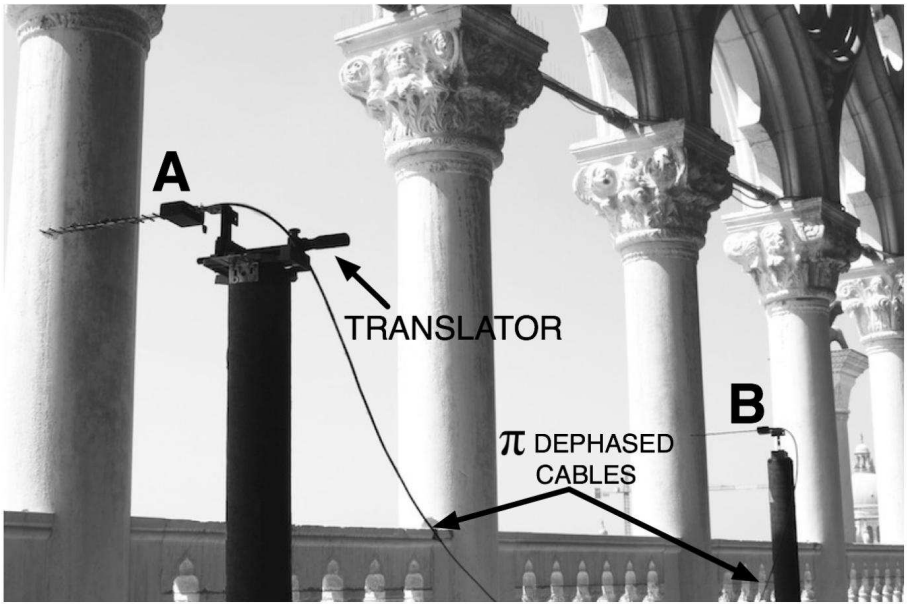

Figure 3.6: Phase difference interferometer: two identical Yagi-Uda antennas are connected together with a 180°-dephased cable through a power-combiner adder module.

orthogonal horizontal direction only.
The interferometer measured the phase difference between the two antennas, A and B, and therefore characterized the spatial phase properties of the beams, i.e. the fingerprints of the vorticity OAM states of the field. To discriminate the two different spatial modes of the electromagnetic field, we aligned antenna A, antenna B and the field singularity along a line parallel to the horizon, and the singularity was positioned in the middle of the segment delimited by antennas A and B (figure 3.7). If the setup were perfectly aligned, the twisted electromagnetic wave with $\ell = 1$ would have shown an exact 180° azimuthal phase difference between the two antennas, subsequently compensated by the cable electric delay thus producing an intensity maximum. The untwisted beam ($\ell = 0$), with 0° azimuthal phase difference, would have produced an intensity minimum for the same settings.

Electromagnetic waves with wavelength λ, propagating along the two paths from the source to the two receiving antennae A and B, acquired a total phase difference ϕ that depended on:

- the angle θ between the incident plane wavefront and the interferometer baseline,
- the relative azimuthal term between the two receiving antenna ϕ_ℓ due to the beam vorticity ($\phi_\ell = 0$ when $\ell = 0$, $\phi_\ell = \pi$ when $\ell = 1$),
- a generic additional spatial/temporal phase term ϕ_0 introduced by

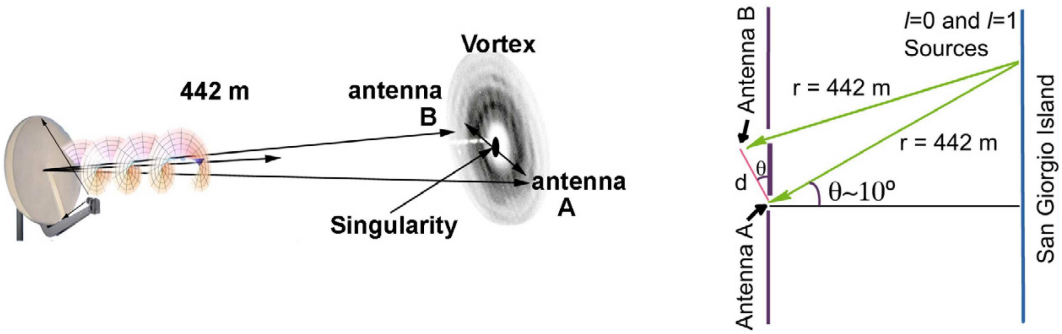

Figure 3.7: Sketch of the experiment in San Marco (not to scale). From left to right: the transmitting antenna, the twisted radio beam and the two antennae A and B aligned with the singularity of the beam. The two receiving antennae were positioned so that the singularity was located on the baseline between the two antennae at the midpoint of the segment AB. Rightmost panel: schematic representation of the experiment.

the experimental setup (e.g. cable delay, imperfect parallelism of the receiving antennae, etc.).

This total phase difference can be approximated by:

$$\phi = 2\pi \frac{d \sin\theta}{\lambda} + \phi_\ell + \phi_0 \tag{3.4}$$

where d is the separation of the two receiving antennas. The signal was collected equally by antennae A and B in phase and the signal of antenna A arrived at the signal adder 180° out of phase with respect to that of antenna B because of electric $\lambda/2$ cable delay, resulting in a difference signal configuration, $\mid A - B \mid$, such that

$$\mid V_A - V_B \mid \approx \mid V_0 - V_0 e^{i\phi} \mid = 2V_0 \sin\left(\frac{\phi}{2}\right) \tag{3.5}$$

where V_0 is the voltage measured at the antenna cable end (receiver input). A maximum is obtained when $\phi = (2k+1)\pi$ and k is an integer.
By adding a phase delay to the signal from antenna A, one can change the pointing direction of the antenna system in such a way that the segment $A-B$, delimited by the two antennae, would effectively rotate rigidly around the field singularity in the horizontal direction orthogonal to the propagation of the electromagnetic signal, with the result of moving the position of the null interference fringes and compensating for the presence of additional phases and the inclination of the interferometric base with respect to the direction of the source. Alternatively, a similar compensation is obtained by moving antenna A along the direction of the source by a quantity

$$\Delta x = \frac{\lambda n}{2\pi}. \tag{3.6}$$

Consequently, if we consider the $\ell = 0$ signal, ϕ_ℓ is null and the phase difference between the two paths can be written as

$$\phi = 2\pi \frac{d \sin\theta}{\lambda} - n. \tag{3.7}$$

The bearing to the transmitter for $\ell = 0$ is, in the ideal case, determined by a minimum or total absence of signal. The parameter n can be adjusted to improve the tuning of the receiving system and read a signal minimum in the exact direction to the transmitting antenna. Here, n is negative when antenna A is moved towards the source.
If the beam carries OAM, the phase distribution of the wavefront arriving at antennae A and B will exhibit a characteristic topological signature and ϕ_ℓ will be different from zero. In the simplest case, when the centre of the vortex coincides with the centre of the interferometer and ϕ_0 is negligible, the two antennae will experience a phase gap due to the OAM of the electromagnetic wave $\phi_\ell = \ell\pi$ and a maximum of the signal is obtained when the phase factor is:

$$\phi = 2\pi \frac{d \sin\theta}{\lambda} - n + \ell\pi = (2k+1)\pi, \qquad k \in \mathbb{Z}, \tag{3.8}$$

where $\mathbb{Z}$ is the set of all integer numbers. Considering the case where, if we do not move antenna A, the interferometer basis is parallel to the incident plane wavefront, the first term of equation (3.8) is null. When $\ell = 1$, a maximum for the vortex is achieved when $n = 0$ and $k = 0$. Because of destructive interference due to the 180°-dephased cable connecting antenna A and antenna B, the $\ell = 0$ signal intensity will at the same time experience a minimum. On the other hand, a maximum for the $\ell = 0$ mode will be obtained when $n = -\pi$, thus, from equation (3.6), when $\Delta x = -\lambda/2$, corresponding to a minimum for the vortex. Following these considerations, we aligned the interferometer so as to have the field singularity at the midpoint of the line joining the two receiving antennas (i.e. the interferometer basis) and obtained a phase gap ϕ_ℓ between the two antennae. To better optimize the interference fringe structure we oriented the baseline by an inclination $\theta \sim 10°$ with respect to the balcony in order to be orthogonal to the incoming beam (figure 3.7).

In order to have a simple, straightforward and practical method to discriminate between the two orthogonal OAM channels, transmitted on the same carrier frequency, we frequency modulated them with constant-level audio signals at different modulation frequencies (400 Hz and 1000 Hz for the untwisted and twisted wave, respectively) by injecting a -5 dBm monophonic audio signal in the video band of each transmitter. The

thus-modulated radio signals were received by the two Yagi-Uda antennas, summed by a beam adder module (a 3 dB power splitter/combiner Mini-Circuits ZX10-2-42+) and then re-converted (demodulated in the FM receiver) into monophonic audio signals, that were subsequently digitally sampled, recorded and analyzed in real time with 32-bit resolution. Each dataset so produced was 22870008 bytes long.
The total signal loss measured in the receiving line of the interferometer was 6 dB (we attribute it to cables losses and to the use of the 3 dB beam adder module). In order to reduce the power of the signal we inserted a 10 dB attenuator into the receiving line so that the audio digitizer connected to the receiver output would not saturate due to overvoltage. In a conventional single-antenna receiver setup that detects linear momentum only, the two radio signals were audible simultaneously. By mechanically moving the antenna A with respect to B to select one of the two orthogonal OAM beams, one signal was alternately suppressed with respect to the other due to the different spatial phase signature of the two OAM states. We adjusted the baseline in order to optimize the discrimination of the two different OAM channels by moving antenna A.
Since a FM (frequency modulation) transmission has the property of generating a constant amplitude output, we adjusted the output of the two transmitters to measure the same receiver output voltage, 1 VCC (Volt in continuous current) for each channel. In this way we were able to characterize the transition between equal-intensity twisted and untwisted channels. Figure 3.8 shows the voltage of the signal measured at the output of the antenna receiver and amplifier. The untwisted beam (line marked 'o') showed destructive interference in the interval 8.5-9.4 cm (approximately 0.7λ - 0.8λ) from the initial antenna position. In the corresponding audio track, the carrier disappears and the 400 Hz tone is suddenly replaced by white noise, which appears louder due to the automatic gain control (AGC) of the receiver. This is a clear indication of destructive interference. Similar behavior was observed in two other smaller regions and is possibly due to effects of the secondary Yagi lobes that were not considered in our autocorrelation analysis. The twisted beam (red continuous line), on the other hand, presented a richer forest of alternating maxima and minima due to the sampling of the field from a finite-sized antenna; only near the initial position of the antenna (0.4 - 1.6 cm) a wide region of total destructive interference was observed. The inner boundaries of the two main minima regions (from the initial position of the antenna, these regions are at 0.4-1.6 cm for $\ell = 1$, and at 8.5-9.4 cm for $\ell = 0$) are separated in distance by half a radio wavelength, as we predicted from equation (3.8).
In figure 3.9 we display the audio frequency spectrum, from 0 to 3 kHz, of the two separate OAM channels ($\ell = 0$, upper panel; $\ell = 1$, middle

panel) obtained from the best acquisition made during our OAM tuning experiments. Each single channel is said to be tuned when the other one experiences destructive interference and the corresponding audio tone disappears. In the lower panel we show the spectrum of the superposed $\ell = 0$ and $\ell = 1$ channels, measured outside the regions of destructive interference. This result is confirmed by the Tolonen-Karjalainen autocorrelation for multi-pitch detection[7] [87], as shown in figure 3.10. Whereas the $\ell = 0$ mode always shows a clear autocorrelation, the $\ell = 1$ mode always presents a series of harmonic tones at higher frequencies (due to the imperfection of the hardware we were using).
We recorded three MP3 audio files of the tuning between the two OAM channels, that are provided as additional material in our publication "Encoding many channels on the same frequency through radio vorticity: first experimental test" [78], available online at http://iopscience.iop.org/1367-2630/14/3/033001. The first audio file is the recording of the spatial tuning of the channel without OAM only. One can hear the main tone at 400 Hz and then strong white noise in the position where antenna A, moving in the direction of the source with respect to antenna B, reaches the point where the signal is cancelled by the interferometer. The second file shows that the twisted beam has a much richer spatial structure than that of the untwisted beam. Finally, the third file is the recording of the vortex tuning between the two different OAM states transmitted simultaneously on the same frequency and used in the data analysis reported in figures 3.8, 3.9 and 3.10.
Already with this setup, one can obtain four physically distinct channels on the same frequency by additionally introducing the use of polarization (which is related to the spin angular momentum, SAM), which is independent of OAM.

3.5 Conclusions

Our experimental findings confirm that the spatial phase signature is preserved even in the far field region and for incoherent non-monochromatic wave beams. These results open up new perspectives both for wireless communication and for physics and astronomy: we can hope to detect OAM in the light coming from astrophysical sources, and get new information about the sources [81] and the traversed interstellar medium [80].

[7] We used sound techniques because we had audio signals, and not digital signals.

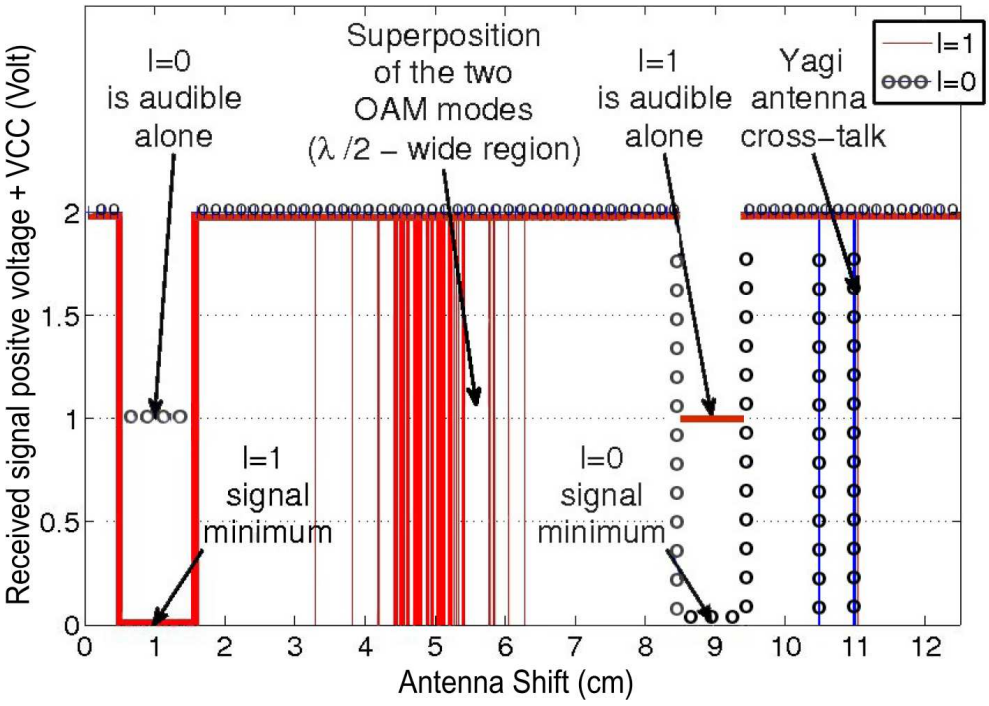

Figure 3.8: Diagram of the monophonic audio recordings of the twisted/untwisted beams. The output of the two transmitters was adjusted to ensure the same maximum input voltage of 2 V when both channels were present, and 1 VCC max for each individual channel. The first minimum is found at about 1 cm of antenna shift for the $\ell = 1$ mode (continuous line). Here the $\ell = 0$ channel (marked with symbol 'o') has a maximum and the associated audio tone is clearly audible. The same was found for the $\ell = 0$ mode around the 9 cm antenna position. The inner boundaries of the two minima regions are separated in distance by half a radio wavelength. Between these positions there was a forest of minima of the $\ell = 1$ mode, a phenomenon due to the sampling of the field from a finite-sized antenna. Beyond the minimum located at 9 cm, two additional alternating signal minima due to the cross-talk of the two Yagi-Uda antennae were found.

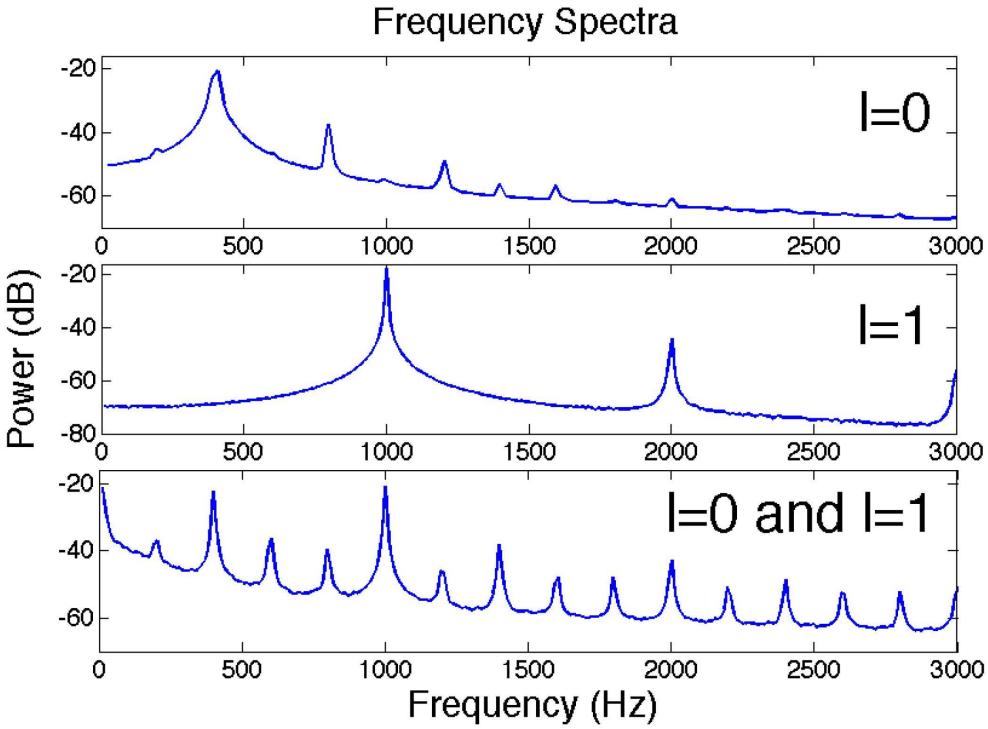

Figure 3.9: Spectral analysis of the demodulated audio signal when the antenna interferometer was tuned by the spatial motion of one antenna to receive two independent and superposed OAM modes in the same frequency band. The spectra are truncated at 3 kHz for better clarity. Upper panel: audio frequency spectrum of the beam in the region where the interferometer is tuned for the $\ell = 0$ mode signal. Clearly visible is the main peak at 400 Hz followed by the higher-frequency harmonics. The power of the signal is distributed with decreasing power at higher frequencies. Middle panel: audio spectrum in the position where only the $\ell = 1$ mode audio signal is audible. Also in this case the power is distributed with less power for higher-frequency harmonics of the 1 kHz main frequency. In both the two spectra there are no spurious frequencies introduced by the other signal. Lower panel: audio spectrum of the signal where the two beams ($\ell = 0$ and $\ell = 1$) are not separated. Both the audio frequencies are visible.

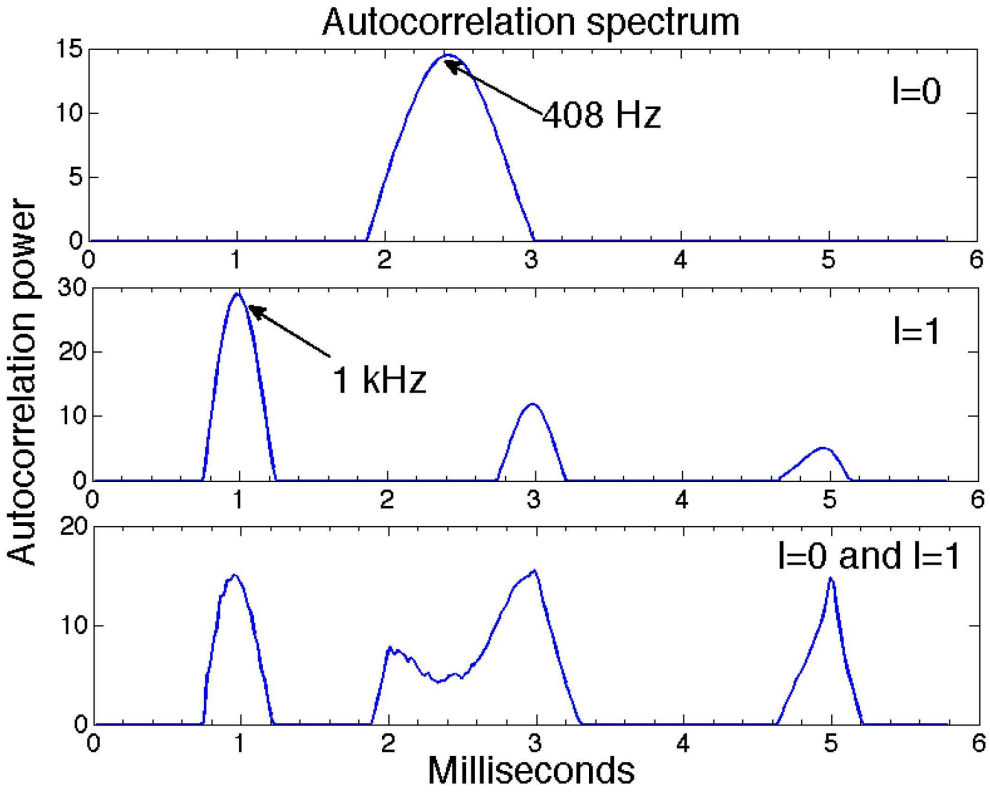

Figure 3.10: Autocorrelation spectral analysis of the audio transmission in three different antenna positions. Upper panel: the $\ell = 0$ mode ($\sim$408 Hz) detectable when the antenna is at a position between 0.4 and 1.6 cm. Middle panel: the $\ell = 1$ (1 KHz), from 8.5 cm to 9.4 cm, with the exception of the two small intervals where a cross talk of the two antennae was observed. In the lower panel, the superposition of both the audio signals at 400 Hz and 1 kHz is clearly evident, showing the impossibility of separating the two channels when the moving antenna is in the interval 1.8 - 8 cm.

3.6 Appendix: technical details

Hardware

To demonstrate the feasibility of implementing multiple radio communication channels on the same frequency, discriminated only by their OAM, we adopted a very basic hardware configuration, comprising a couple of commercial audio/video tuneable receiver and 2W transmitter modules feeding the twisted parabolic antenna for the twisted beam with OAM ($\ell = 1$), and a 16.5 dBi Yagi-Uda antenna for beams without OAM ($\ell = 0$) (figure 3.5). The COTS receiver was connected to two identical 12-element, 16.5 dBi gain Yagi-Uda antennae (figures 3.11, 3.12 and 3.13), tuned to 2.4 GHz and mounted on the top of two identical plastic columns ($\varepsilon \approx \varepsilon_0$). The baseline between the receiving antennae was 4.50 m, with laser-controlled levelling and calibrated mutual distance. Each of the receiving antennae was mounted on a mechanical translator that provided fine-tuning in an interval of 10 cm ($\sim 0.8\lambda$). The cable connections were made with Belden H155 WiFi coaxial cable, 50 Ω impedance and 5.4 mm diameter. The velocity factor in the cable for this type of cable is 79 % with (9.3 dB loss)/(100 m), characterized by the producer at a frequency of 100 MHz. Then, the half-wavelength cable junction used to build the phase difference interferometer resulted to be 4.94 cm long.

Figure 3.11: One of the two receiving Yagi-Uda antennae of the interferometer mounted on the top of an isolated plastic pillar.

For the production of the offset helicoidal parabolic antenna, from a pair of identical, 15° offset, 80 cm diameter steel parabolic antennae, the dish was transformed into a vortex reflector by elevating, from the original shape,

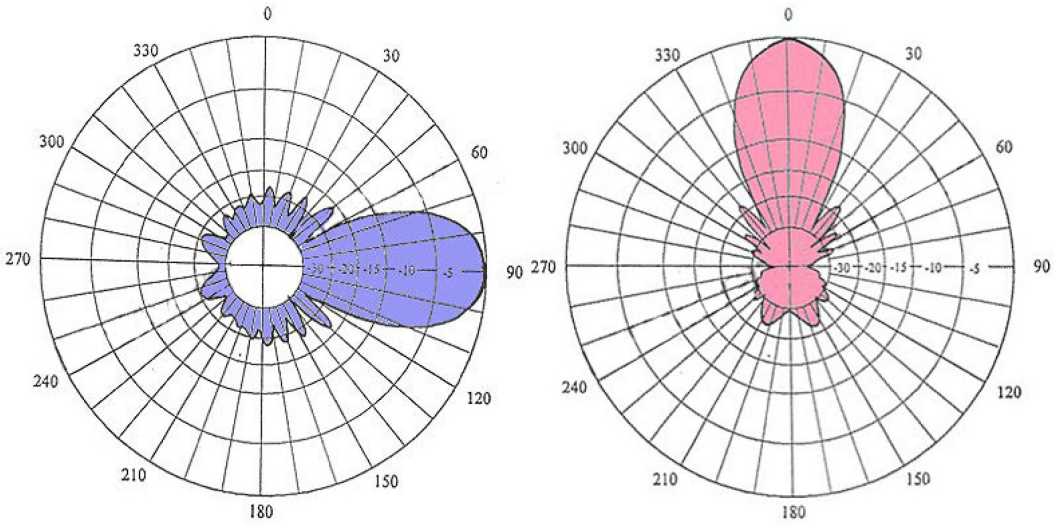

Figure 3.12: Horizontal and vertical linear momentum radiation (Poynting vector) diagrams of the lobes of the COTS Yagi-Uda antennae used in the interferometer.

Operating frequency (MHz)	2400–2480
Average gain	16.5 dBi
Size	$45 \times 5 \times 4$ cm
Vertical/horizontal irradiation	35°
Impedance	50 Ω
SWR (standing wave ratio)	<1.3

Figure 3.13: Main characteristics of the Yagi-Uda antennae used in the experiment.

the surface of one of the two parabolic antennae of the quantity necessary to produce a $\ell = 1$ beam (see equation (3.2)). The main characteristics of the non-helicoidal parabolic antennae used to build the vortex reflector are listed in figure 3.14.

Transmitter/receiver modules

The audio and radio signals used in the calibration and with the actual radio transmission were generated with commercial high-quality super-heterodyne frequency modulating (FM) transmitting modules. The output impedance was 75 Ω. The deviation in frequency relative to the carrier frequency (2.414 GHz) due to the FM modulation (15 MHz) can be considered negligible and not to cause significant distortion of the vortex or a consequent change of the topological charge generated by the twisted parabolic antenna.

dB contour down (degrees)	0	0.25	0.5	1	24	26
Full beamwidth (degrees)	0	3.13	4.42	6.25	8.84	10.83
Gain dBi	24.2	23.95	23.7	23.2	22.2	21.2

Figure 3.14: Main characteristics of an non-helicoidal parabolic antenna lobe width having the same diameter and focal ratio as the twisted parabolic antenna. The theoretical gain is expressed as a function of the angular deviation from the beam direction.

Site of the experiment in Venice

Transmitting station: Torretta della Compagnia della Vela in San Giorgio,
altitude: 10m msl (mean sea level),
latitude: 45°25′48″ N,
longitude: 12°20′35″ E.

Receiving station: Loggetta del Palazzo Ducale,
altitude: 16m msl,
latitude: 45°26′00″ N,
longitude: 12°20′25″ E.

Geometrical distance between the two stations: 442m as measured with GPS and Google Maps.

Electrosmog-Loggia (Lobby) of Palazzo Ducale

The following data are environmental parameters that we measured to be sure that the signals we acquired did not depend on the destructive or constructive environmental resonances.

date: 13 June 2011
time: 9.00 - 9.45 GMT
height of the balcony rail: 130cm
distance between two columns of the lobby: 214 cm
See figure 3.15 and 3.16.

Figure 3.15: Lobby of Palazzo Ducale, 50m long, location of the receiving station.

Loggia 1	**Max (dBm)**	**Avg (dBm)**
2.414 GHz Vpol	−87.5	−88
2.414 GHz Hpol	−89	−89
Loggia 13	**Max (dBm)**	**Avg (dBm)**
2.414 GHz Vpol	−87.9	−89
2.414 GHz Hpol	−88	−89
Loggia 25	**Max (dBm)**	**Avg (dBm)**
2.414 GHz Vpol	−86	−87
2.414 GHz Hpol	−88	−88

Figure 3.16: The electrosmog background measured in the lobby of Palazzo Ducale (vertical and horizontal polarizations).

Chapter 4

Detection of the orbital angular momentum of light from astrophysical sources

In the previous chapters we have discussed the possibilities of getting new information about the universe thanks to the study of the orbital angular momentum of light, and we have reported an experimental demonstration about the propagation and conservation of OAM in the far field region and for incoherent non-monochromatic wave beams. If OAM can be a new astronomical observable carrying astrophysical information, and if this information is preserved during its propagation, next step is trying to measure OAM enclosed in light collected by astronomical telescopes.
Up to know OAM has been generated, created, observed, analyzed and exploited in several fields such as radar [64], nanotechnology [30] and quantum experiments [93]. In astronomy and space sciences it has been used to improve the resolving power of diffraction-limited optical instruments [77] and coronography [24]-[49], but it has never been measured in light coming from the sky as a new observable containing new information. Even if theoretical works demonstrate that it could be produced by some astrophysical processes [31, 80, 81] , it has never been detected and used as a new diagnostic instrument for celestial light.
The first step towards this direction is the construction of astronomical devices able to detect the orbital angular momentum enclosed in the collected light. In this chapter we are going to analyze a possible way to detect OAM with optical telescopes.

4.1 Introduction

Several methods to measure orbital angular momentum of light have been studied in the past:

- the interference of a beam containing an optical vortex with a flat wave front results in an interference pattern with a fork-like structure that reveals the topological charge of the vortex [63, 74] (e.g. diffraction pattern from a triangular aperture [14, 27, 36, 76]). However, this method is unfavourable for many applications, in particular for those where the studied beam is spread out over a large area, because it needs an additional extended flat wave front;

- the use of diffractive optical elements (DOEs) containing an ℓ-fold fork dislocation can be used both to generate beams carrying orbital angular momentum [10, 11, 33, 34], and to measure OAM [47]: the forked diffraction grating, which produces an helical mode in the first diffraction order then illuminated with a Gaussian beam, can also be used in reverse to couple light with a helical phase into a single-mode fibre, measuring the power of that mode. For each ℓ value one wants to measure, one needs a different fork hologram with the appropriate dislocation, so to check for N different states, one needs at least N photons;

- similarly, a spiral phase plate and q-plate technology can be used to test whether the input light is in a specific state or not, i.e. they can be used as a filter for orbital angular momentum [51, 59];

- a system of Mach-Zender interferometers and Dove prisms can be used to measure the OAM state, but it's technically very challenging and difficult to implement in large optical systems [45];

- the observation of the rotation of trapped particles in optical tweezers [26, 32];

- the rotation of a beam with OAM, which shifts the frequency [22].

However, all these methods are not appropriate for detecting OAM enclosed in light coming from astronomical objects, and a way to measure efficiently the distribution of ℓ values contained within light has presented a challenge for many years. Astronomical observations of the orbital angular momentum of photons have apparently never been attempted, with the exception of the work of Uribe-Patarroyo et al. in 2010 [90], where they tried to measure the OAM spectrum of light from an extended source, the Sun, but they didn't succeed.

Recently, a method to measure the light orbital angular momentum spectrum using an optical geometric transformation has been developed, the so-called *orbital angular momentum mode sorter*[15, 16, 43, 44], which sorts many OAM states at the same time, with a great efficiency ($\approx 100\%$) and is easy to align and operate. For these reasons we have thought to try to adapt it for optical telescopes, so that it can be used also in astronomy, and not only on optical benches.

4.2 The orbital angular momentum mode sorter

In 2010 G. C. G. Berkhout, M. P. J. Lavery et al. ([15, 16, 43, 44]) developed a new method to efficiently sort the orbital angular momentum states of optical light using two static optical elements which map azimuthal coordinates to linear transverse coordinates. For each input OAM state, light is focused to a different transverse position making possible simultaneous measurements over many states, thus performing an OAM spectrum.
The method used in the OAM mode sorter utilizes an optical geometric transformation enabling an efficient spatial separation and subsequent analysis of many OAM states and of their superposition. The intention of the authors was to use this OAM analyzer for communications, which require an efficient and simultaneous detection of light in different OAM states. The same performances are required for the detection of OAM from astronomical sources, since we are interested in analyzing all the OAM components contemporaneously enclosed in the beams of light we collect.

Multiple plane waves can be distinguished by a lens thanks to their transverse phase gradient. Indeed, a lens focuses a plane wave to a spot in its focal plane, whose transverse position depends on the transverse phase gradient of the wave. A requirement for the separation of any two plane waves is an additional phase change of 2π across the aperture of the lens, resulting in a difference in spot positions comparable to the Rayleigh resolution limit. This is the basic idea for the OAM sorter and how it separates different OAM states: a change in the mode index of $\Delta\ell = 1$ corresponds to an increment in the azimuthal phase change of 2π. Therefore, the two key optical elements of the OAM mode sorter are optical components that transform azimuthal positions into transverse positions, i.e. two optical elements that transform a helically phased input beam into a transverse phase gradient output before the beam traverses the focusing lens. Acting together these elements map a position (x, y) in the input plane to a position (u, v) in the output plane, with:

$$u = -a \cdot \ln\left(\frac{x^2 + y^2}{b}\right) \tag{4.1}$$

$$v = a \cdot \arctan\left(\frac{y}{x}\right) \tag{4.2}$$

where a and b are constants related to the size of the optical components, and (x, y), (u, v) are Cartesian coordinate systems. This mapping transforms a set of concentric rings at the input plane into a set of parallel lines in the output plane. Therefore, it transforms the azimuthal phase term $\exp(i\ell\theta)$ into a transverse phase gradient: the phase and intensity of the beam in the form $\exp(i\ell\theta)$ are transformed by the combination of the two refractive optical elements into a complex amplitude at the output plane of the form $\exp(i\ell v/a)$ [1]. A spherical lens placed after this second element then separates the resulting transverse momentum states into specified lateral positions in its back focal plane (s, t), thus allowing for the efficient measurement of multiple OAM states simultaneously. In figure 4.1 one can see the two refractive optical elements which convert orbital angular momentum states into transverse states, while in figure 4.2 one can see the conversion of an helically phased input beam into a transverse phase gradient output and, in the end, into a transverse position related to the OAM value of the input beam.

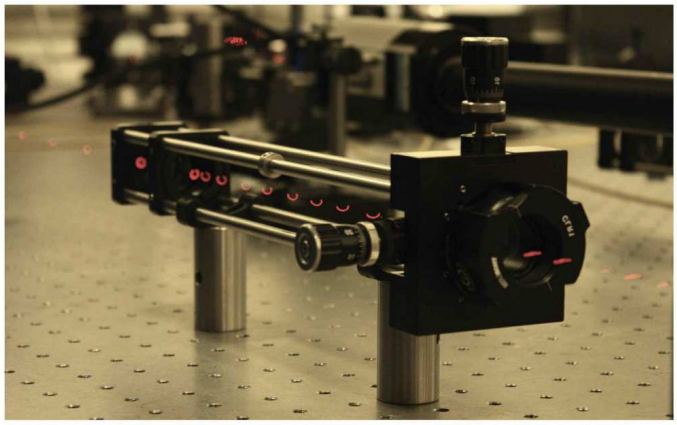

Figure 4.1: Refractive optical elements converting OAM states into transverse momentum states. In red, the image of the beam overlaid to the image of the two optical elements (source: M. P. J. Lavery et al. 2012 [44]).

[1] As it is stated in Berkhout, Lavery et al. (2010) [15], the first optical element is the key one, transforming the azimuthal position in the input beam into a transverse position in the output beam. The resulting variation in optical path length means that the transformation introduces a phase distortion that needs to be corrected by a second element. Therefore, the second optical element, positioned in the Fourier plane of the first, corrects for this phase distortion, so that the the transverse beam obtained with the first element does not closes again into a ring.

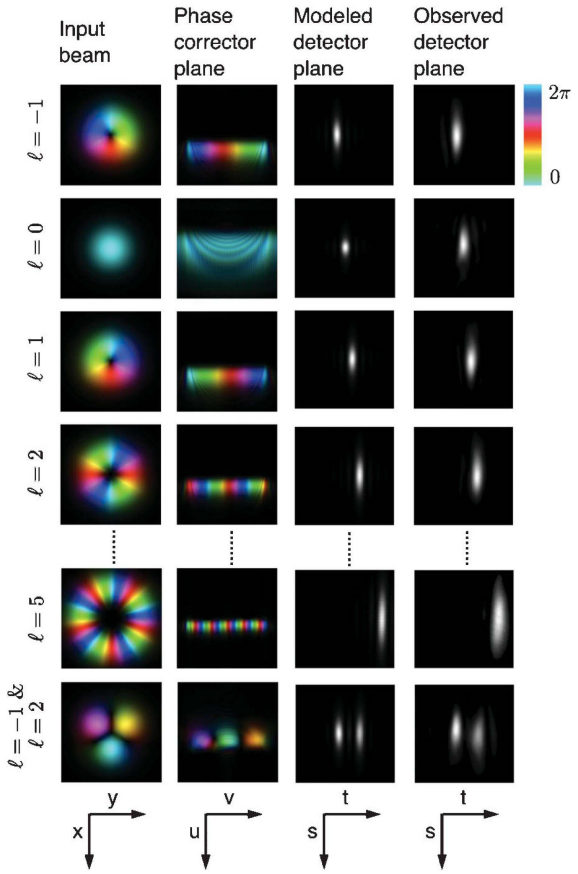

Figure 4.2: Modeled and observed phase and intensity profiles at various planes in the optical system. From left to right, the images show the modeled phase and intensity distribution of the input beam just before the transforming optical element and just after the second optical element, and the modeled and observed images in the CCD plane for five different values of ℓ. The final row shows the results for an equal superpositions of $\ell = -1$ and $\ell = 2$. The last two columns are 6× magnified with respect to the first two columns (source: G. C. G. Berkhout et al. 2010 [15]).

4.3 The OAM mode sorter for optical telescopes

Since the OAM mode sorter efficiently performs the OAM spectrum of light, it paves the way to interesting astrophysical investigations which make use of the OAM state basis. However, the OAM mode sorter is an instrument built to be used with laser light on optical benches, so in controlled conditions. We tried to adapt it in order to be mounted on the focal plane of a telescope, with the aim of performing the OAM spectrum of light coming from the sky. This work is the result of a period spent at the University of Glasgow, with the Optics Group of the department of Physics and Astronomy.

OAM mode sorter configuration for the telescope

Firstly, we configured the OAM mode sorter for a 19 cm telescope, than can be seen in figure 4.3.

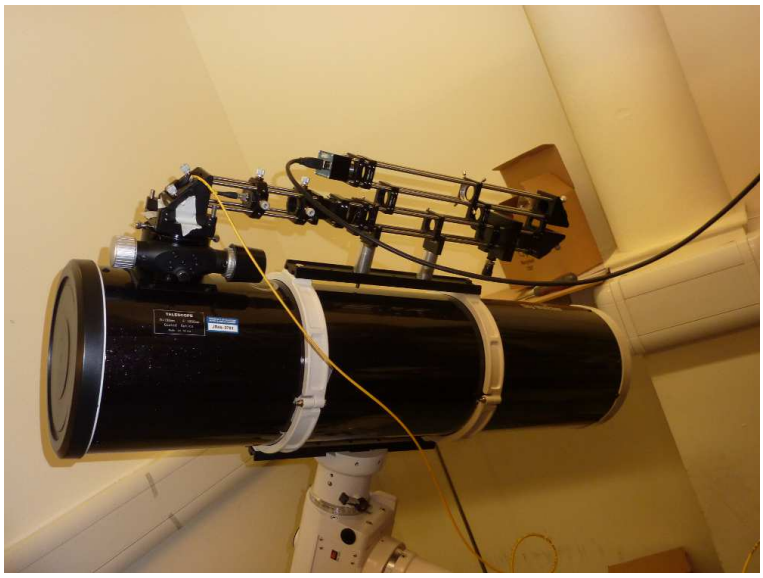

Figure 4.3: The 19 cm telescope we used for the first tests to adapt the OAM mode sorter to an optical telescope. To align the OAM mode sorter, we used a Laguerre-Gaussian beam entering in the sorter through a fiber (the yellow cable).

The telescope was a Maksutov-Newtonian reflector telescope, with the following characteristics:

- f-number: $f/5.3$
- diameter of the primary mirror: $D = 19$ cm
- diameter of the secondary mirror (the central obstruction): $d = 50$mm (26%)
- focal length: $f_{telescope} = 1$ m.

In figure 4.5 one can see the optical elements constituting the OAM mode sorter:

1- element Ap: it is a pinhole aperture, placed on the focal plane of the telescope, at a distance f_A from lens A;

2- element A: it is a focusing lens, with focal length f_A and at a distance f_A from the initial pinhole aperture and the first refractive element of the mode sorter, $S1$;

3- elements $S1$ and $S2$: they are the two refractive optical elements performing the azimuthal to linear-transverse coordinates transformation, they are the core of the OAM mode sorter which convert orbital angular momentum states into transverse momentum states. The distance between them is 30 cm and depends on the wavelength;

4- element B: focusing lens, with focal length f_B;

5- elements $M1$, $M2$, $M3$: flat mirrors tilted 45° with respect to the incident beam;

6- element $Micro$: microscope objective at a distance f_B from lens B, with a 20× magnification and focal length f_{Micro};

7- element $Filter$: 633 nm filter;

8- element CCD: CCD camera, at a distance f_{Micro} from $Micro$.

We want to describe these elements.

1- The pinhole aperture Ap is necessary to filter the Poynting vectors: since now we are dealing with light from astrophysical sources (and not from lasers), the OAM spectrum has a very large bandwidth. Therefore we need to filter the Poynting vectors, otherwise we could detect a flat spectrum just because we are collecting only a little portion of a spectrum with a large bandwidth.

2- Lens A has the function to reduce the beam size, which has the dimension of the primary mirror of the telescope, and must be reduced before passing through $S1$. It is at a distance $f_{telescope} + f_A$ from the 19 cm collecting mirror of the telescope, in order to make a telescope configuration implementing the right demagnification (demagnification: $M = f_{telescope}/f_A$). We chose $f_A = 7.5$ cm in order to have the output beam with the dimensions appropriate for the two optical lenses $S1$ and $S2$ of the OAM mode sorter (they worked best with an input beam waist value w_0 between 1.2 cm and 1.9 cm).

3- $S2$ is mounted on a translator, because our degrees of freedom for the alignment of the OAM mode sorter with respect to the optical axis of the telescope [2] were mirror $M1$ and lens $S2$. We decided to use $M1$

[2]The optical axis of the OAM mode sorter has to be aligned with the optical axis of the telescope. Indeed, as we discussed in chapter 1, the OAM value depends on the reference axis and a parallel lateral displacement of the incoming beam combined with a tilt (with respect to the optical axis of the sorter) significantly changes the OAM spectrum (see next section). Therefore it is essential that the sorter is stable and aligned to the axis of the incoming beam.

and $S2$ because for a good alignment we have to use two decoupled degrees of freedom. The best way for this condition to be verified is having the degrees of freedom in two different planes, one on a focal plane and the other on an image plane.
The distance between the transformation elements S_1 and S_2 depends on the dispersion in the PMMA constituting these two refractive elements, as one can see in figure 4.4. In our case we were using a filter making pass only red light with $\lambda = 633$ nm, thus the right distance was 30 cm.

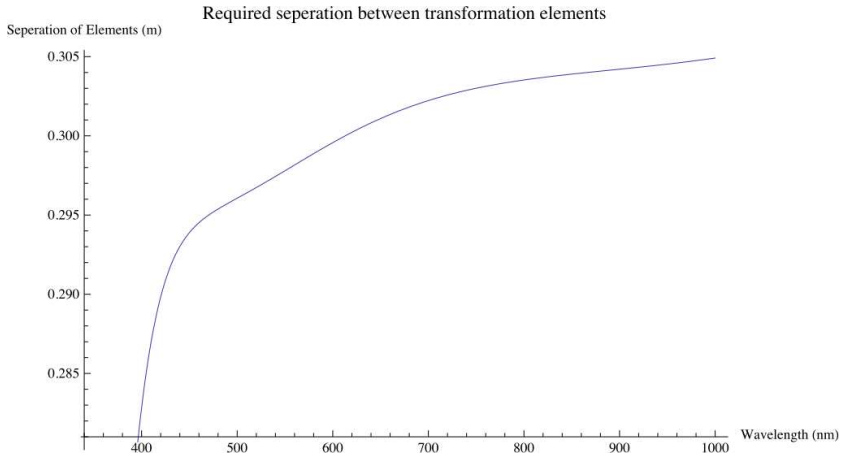

Figure 4.4: Required distance between the two transformation elements of the OAM mode sorter as due to the dispersion in the PMMA they are made of.

4- B is a spherical lens placed after lens $S2$, that separates the resulting transverse momentum states into specified lateral positions in its back focal plane, thus allowing for the efficient measurement of multiple OAM states simultaneously, so performing the OAM spectrum. The transverse position of spots at the back focal plane, t_ℓ, changes as a function of ℓ, following the relationship:

$$t_\ell = \frac{\lambda f_B}{d_B}\ell \tag{4.3}$$

where $d_B = 18mm$ was the diameter of the lens.

5- $M1$, $M2$ and $M3$ are flat mirrors, that we decided to use in order to make the sorter laying on the tube of the telescope and not hanging on the eyepiece. In this way it was more stable during the tracking of the telescope.

6- The microscope objective is used to distance the spots on the camera, corresponding to different ℓ values of the incoming beam. Instead of

using a microscope objective, according to relationship (4.3) one could use a spherical lens with a larger focal length f_B, but we preferred this solution in order not to elongate the rods, to preserve the stability of the OAM mode sorter.

7- Before the camera, we used a 633nm filter (only red light passed through) to protect the camera from external light. We used a 633nm filter because the first tests of the sorter on the telescope were done in laboratory, where the light passing through the sorter was the light of a He-Ne laser, which operates at 633nm.

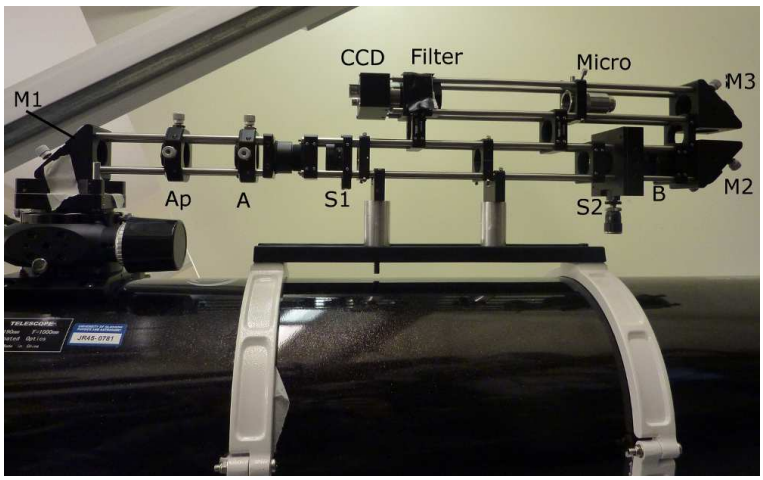

Figure 4.5: The adapted OAM mode sorter on the tube of the 19 cm telescope. *Ap* is a pinhole aperture placed on the focal plane of the telescope, A and B are focusing lenses, $S1$ and $S2$ are the two optical elements performing the azimuthal to linear-transverse coordinates transformation, $M1$, $M2$, $M3$ are flat mirrors tilted 45° with respect to the incoming beam, $Micro$ is a microscope objective, $Filter$ is a 633 nm filter and CCD is the camera.

One of the main difficulties in adapting the OAM mode sorter for a telescope, was not knowing the precise position of the telescope's focal plane. Indeed, even if we knew the focal length of the telescope, we didn't know with high precision at which distance it was from the eyepiece, and therefore we didn't know exactly where lens A had to be placed. The consequence of the lack of this piece of information is an enlargement of the bandwidth of the spectrum. If lens A is not exactly at distance f_A from the focal plane of the telescope, the beam coming out from it and passing through the two transforming lenses $S1$ and $S2$ of the sorter is not collimated, giving rise to a larger bandwidth. However, even if the bandwidth is larger, this does not affect the center of mass of the OAM spectrum.

4.4 Test of the OAM mode sorter at Celado Observatory

After having built an OAM mode sorter for telescopes, we tested it at Celado Observatory. We used the main telescope of the observatory, a Newtonian telescope with the following characteristics:

- diameter of the primary mirror: $D = 800$ mm
- focal length: $F = 3200$ mm
- 6 focal positions
- location: latitude N 46° 5' 59. 99",
  longitude E 11° 4' 0. 00",
  altitude 1260 m

Figure 4.6: The 80cm Newtonian telescope at Celado observatory.

We were able to detect data only one night, on 22^{nd} September 2012, because we spent the previous two nights for the tricky procedure of aligning the sorter. The alignment of the sorter with the source (in our case with the optical axis of the telescope) is very important because, as M. V. Vasnetsov et al. demonstrated in 2005 [92], a misalignment of the incoming beam with respect to the optical axis of the OAM mode sorter can change the OAM spectrum. The effects are of two types:

- if the beam undergoes a parallel lateral displacement, or a tilt (with respect to the optical axis of the sorter), as a consequence a bandwidth enlargement takes place, but the center of mass of the OAM spectrum is not affected;

- if the beam undergoes both a parallel lateral displacement and a tilt, the spectrum is affected both by an enlargement of the bandwidth and by a shift of the center of mass.

On a focal position of the telescope, we mounted the adapted OAM mode sorter, as can be seen in figure 4.7. To detect the spectrum, at the end of the sorter we used a high sensibility CCD Watech camera.

Figure 4.7: The OAM mode sorter mounted on one of the six focal positions of the 80cm-Newtonian telescope.

Our first aim was simply testing our OAM mode sorter outdoor and with the light of stars, instead of in laboratory with laser light. For this reason the stars we decided to observe were simply bright stars, with no predicted OAM in their light. We were simply interested in detecting the first OAM spectra from celestial objects, even if these spectra were probably centered on a OAM value equal to zero.
In figure 4.8 there is the list of the stars we pointed, the local times and exposure times of their observations, their geometric altitudes and their apparent visual magnitudes. We decided to observe these stars because of their brightness. The seeing was $\sim$ 1.5 arcseconds. For these observations

we replaced the 633nm filter used with laser light, with a 532nm filter. Consequently, we optimized the OAM mode sorter for this wavelength, changing the distance of the two refractive lenses S_1 and S_2 according to figure 4.4.

OBSERVED STAR	LOCAL TIME	ALTITUDE	EXPOSURE TIME	m_V
Mirphak	02:10	49°54'	3 sec	1.816
Algol	02:18	67°43'	3 sec	2.12
Aldebaran	02:44	41°59'	2 sec	0.985
Aldebaran	04:50	58°12'	10 sec	0.985
Betelgeuse	04:57	42°33'	0.2 sec	0.42
Rigel	05:10	33°11'	0.6 sec	0.12
Sirius	05:17	17°43'	0.5 sec	-1.47
Procyon	05:25	5°11'	0.7 sec	0.34

Figure 4.8: List of the pointed stars, with local times and exposure times of their observations, their geometric altitudes and their apparent visual magnitudes given by the online Simbad catalogue (http://simbad.u-strasbg.fr/simbad/sim-fbasic).

In spectroscopy, a spectrum shows the photon counts[3] (y-axis) for each frequency (x-axis). Similarly, an OAM spectrum detected with an OAM mode sorter shows the CCD counts (y-axis) for each transverse position[4] (x-axis), thus for each OAM value (as expressed by equation (4.3)).
In figure 4.9 there is a comparison among the OAM spectra that we detected. The ordinates have been calculated averaging the CCD counts referred to pixels with the same abscissa, and then normalizing each spectrum, dividing each y-value for the maximum y-value of that spectrum. The spectra have been translated in order to have their maxima overlapping at the same coordinates. One can notice that the half-spectra to the right of the central peaks have always more light than those to the left. It seems to be a systematic error, so we think that it was probably due to some internal reflections. Because of this, one has to compare the left half-spectra. One can see that in general the broadening get smaller at higher altitudes, apart from Algol, which is the highest but also one of the broadest: probably we just took the spectrum in a bad way (it was one of the firsts we took).

[3]If the data reduction has been performed, a spectrum shows the intensities or energy densities or fluxes.

[4]Transverse to the reference axis of the sorter.

4.5 Conclusions and future steps

Since our test at Celado observatory has been the first time someone tried to detect an OAM spectrum from astronomical sources (except for the efforts of Patarroyo et al. in 2002, but they didn't succeed [90]), our aim was just to test the performances of the OAM mode sorter when applied to a telescope, with celestial light. The plot in figure 4.9 shows that the OAM mode sorter works even under these conditions: indeed, we can observe a general trend for the bandwidth, to get larger when the geometric altitude of the stars reduces, which is in accordance with the trend predicted by Rodenburg et al. [68]. Following the theoretical work of Paterson in 2005 [65], they simulated in laboratory the atmospheric turbulence, which was modeled as a randomly varying phase aberration that obeys the statistical spread postulated by Kolmogorov turbulence theory.
The main problem of OAM in the optical domain are the effects of propagation through random aberrations on coherence. For OAM detection, what one needs is the spatial coherence of the beam, therefore the decoherence effect of atmospheric turbulence cannot be neglected. If b is the beam width, and r_0 the Fried parameter, what Paterson stated [65] and Rodenburg et al. found with simulations [68] is that for $b << r_0$ the effects of the phase aberrations are weak and the OAM scattering is small, but they increase rapidly as b becomes comparable to r_0 (see figure 4.10).
The trend showed by our plot in figure 4.9 seems to be in accordance with the predictions of Paterson and Rodenburg [5]. Indeed, when stars approach the horizon, the atmosphere becomes more and more turbulent, corresponding to smaller values of the Fried parameter, and the bandwidth gets larger, i.e. the OAM scattering increases. Thus, we can affirm that the OAM mode sorter applied to a telescope works, and our test can be considered a feasibility study for an instrument able to perform the OAM spectrum of light from celestial objects.

Future steps

Atmospheric turbulence has recently been added to the list of mechanisms for the formation of OAM in traveling optical waves [48, 60, 69, 70]. In order to get rid of the atmospheric effects on the OAM spectra, and to get information about the astrophysical sources or the interstellar medium traversed by light, next step could be *differential interferometry*. We could build another sorter, in order to point at the same time two astrophysical objects (the object we are interested in and a reference one) which are in the

[5] In our case the beam width b is determined by the diameter of the telescope, D.

same isoplanatic angle[6]. Then, the two OAM spectra should be subtracted to reveal any change in the spectrum due to astrophysical processes and not to the atmosphere.

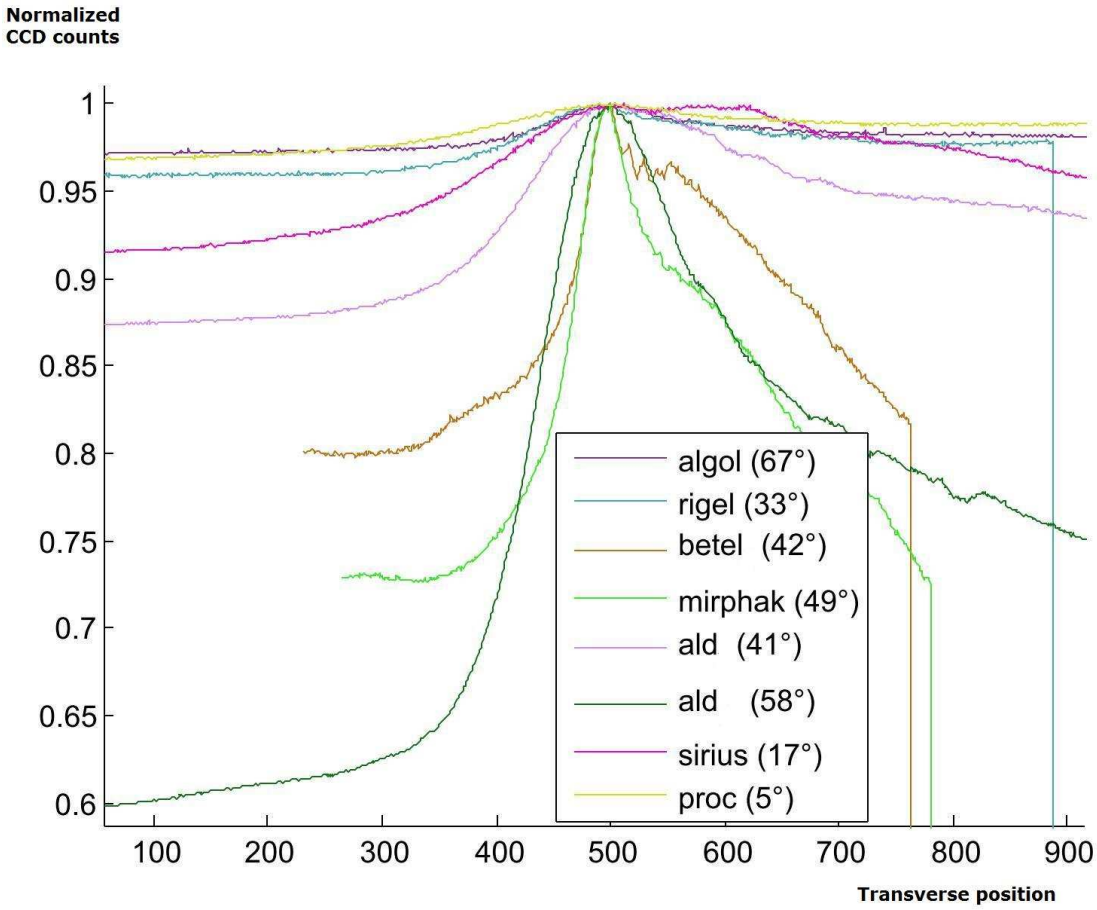

Figure 4.9: Spectra comparison. X-axis: transverse position with respect to the reference axis of the sorter. Y-axis: normalized CCD counts. In the box, there is a legend associating different colors to the different observed stars (some of their names have been abbreviated), with their geometric altitudes in brackets.

[6]In adaptive optics, the *isoplanatic angle* is the angle from the reference star where the correction is still effective.

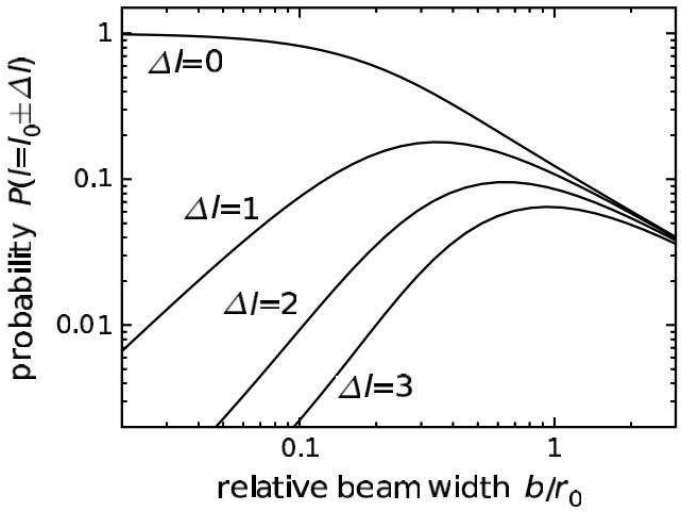

Figure 4.10: Probabilities of obtaining different OAM measurements $P = l_0 \pm \Delta l$ for a LG_1^0 beam plotted against the ratio of the Gaussian beam width parameter b to the Fried parameter r_0. The probability of obtaining the original l value ($\Delta l = 0$) decreases rapidly as the Fried parameter becomes comparable to the beam width parameter. There is a corresponding increase in the probabilities of obtaining OAM measurements different from the initial eigenvalues ($\Delta l \neq 0$), with those corresponding to adjacent azimuthal modes increasing most rapidly (source: Paterson 2005 [65]).

Chapter 5

Conclusions

This thesis highlights the relevance of the study of the orbital angular momentum (OAM) of light in the field of astronomy. Up to now astronomers have not considered this observable, extracting all the information about the radiating Universe by the study of the intensity, frequency and polarization of the light that we receive. Showing that orbital angular momentum can carry information of astrophysical interest, we propose to the astronomical community to consider OAM as a new carrier of information and to study the way it could be detected.

If we consider a reference frame with cylindrical coordinates, where the z-axis corresponds to the direction of propagation of the considered electromagnetic beam, we have demonstrated that media characterized by a perturbed density in the azimuthal component impose orbital angular momentum to the beam passing through [80]. When the electron number density of a plasma exhibits certain spatial properties, such as vortices, any photon has an associated virtual mass term that is smaller than that expected from Proca equations in a homogeneous plasma, because of a negative term that corresponds to a precise orbital angular momentum component. In this case, a cascading process of OAM transfer between the plasma and the photon beam can be achieved, which is related to the electron number density function. Therefore, studying the OAM of light we collect with our telescopes could give additional information about the spatial structure of the interstellar medium traversed by photons during their travel from the source to the observer.

Our experimental findings demonstrate that the spatial phase signature, namely the fingerprint of orbital angular momentum, is preserved even in the far field region and for incoherent non-monochromatic wave beams [78]. These results confirm that new perspectives are opened for astronomers: if

we can affirm that OAM is preserved when traveling in vacuum or homogeneous media, then the OAM fingerprint imposed by interstellar media or other astrophysical processes (such as Kerr black holes)[1] is preserved in its travel to the observer.

Finally, our attempt to adapt an OAM mode sorter to a telescope and our tests at Celado observatory, show that this kind of approach could pave the way to the first detection of the orbital angular momentum of light from celestial objects.

As future steps, we suggest to use at the same time two OAM mode sorter fitted to an optical telescope, performing *OAM differential interferometry*. Pointing simultaneously two stars in the same isoplanatic angle, and subtracting one spectrum by the other, we could get rid of the effects given by the turbulent atmosphere. In this way, the spectrum left should be the result of astrophysical processes, and not due to the atmosphere distorting the wave front.

[1]The orbital angular momentum imposed by the interstellar medium can be discerned by the orbital angular momentum imposed by the space-time dragging around a Kerr black hole because of chromaticity: the former depends on the frequency of the electromagnetic beam, the latter is the same for all the spectrum.

Appendix A

Spin

In physics, spin is related to the intrinsic angular momentum of a body, contrary to the orbital angular momentum, which is related to the motion of the centre-of-mass around a point.
In classical mechanics, spin angular momentum is associated to a rotation of a body around its own centre-of-mass.
In quantum mechanics spin is connected to the intrinsic angular momentum associated to particles. The spin of an elementary particle is an intrinsic physical property, akin to the particle's electric charge and the rest mass. Differently from rotating objects described by classical mechanics, which derive their angular momentum from the rotation of the parts they are constituted of, in quantum mechanics spin is not associated with any internal structure. For example, elementary particles (such as electrons) have spin, even if they are point particles.
Spin is not expected by the quantum mechanics non-relativistic theory, and is introduced as a postulate. It is expected instead by the quantum mechanics relativistic theory (Dirac equation). The value of the spin quantum number s for an elementary particle depends only on the type of particle, and cannot be altered in any way (in contrast to the spin direction). The spin angular momentum S of any physical system is quantized. The allowed values of S are:

$$S = \hbar\sqrt{s(s+1)}$$

where $\hbar$ is the reduced Planck's constant.
Particles with integer spin quantum number (photons with $s = 1$ or the hypothetical graviton with $s = 2$) correspond to bosons, and particles with half-integer spin quantum number ($s = 1/2$ for electrons, neutrinos and quarks) correspond to fermions.
Quantum mechanics states that the spin angular momentum components measured along any direction (for example along i-axis) can take only the

following values:

$$S_i = s_i \hbar$$

where s_i is the spin projection quantum number along the i-axis, and it can take on the following values:

$$s_i \in \{-s, -(s-1), -(s-2), ..., s-2, s-1, +s\} \tag{A.1}$$

Conventionally, the chosen direction is the z-axis:

$$S_z = s_z \hbar$$

$$s_z \in \{-s, -(s-1), -(s-2), ..., s-2, s-1, +s\} \tag{A.2}$$

However, the possible values of s_i are not $2s+1$, but only $2s$ because the eigenvalue with $s_i = 0$ does not exist. For example, there are only two possible values for particles with spin 1: $s_z = +1$ and $s_z = -1$. These values correspond to the quantum states with spin pointing to the $+z$ or $-z$ direction respectively.
A pair of spin components along two non-parallel axis are subject to the uncertainty principle:

$$[S_i, S_j] = i\hbar\epsilon_{ijk} S_k.$$

where ϵ_{ijk} is the Levi-Civita pseudotensor. This relation states that if the particle is in a spin state with, for example, the S_z component completely determined, then the direction of the spin component in the xy plane will be completely indeterminate (only the amplitude will be known).

Spin of electrons

Particles with spin can have a magnetic dipole momentum, exactly as an electrically charged body which rotates in a non-homogeneous magnetic field. This applies to electrons as well: if a beam of hydrogen atoms in their fundamental state passes through a non-uniform magnetic field, it separates in two beams, each of them containing half atoms. The observed forces vary for different electrons, and such differences are attributed to spin differences. Therefore, electron spin is typically measured by observing the trajectory in a non-homogeneous magnetic field.
Because of quantum uncertainty applied to spin, we are not able to measure spin components along different axis at the same time. If we measure the spin of an electron along a random axis, we will never find a fractionary spin quantity: we can imagine that the measurement itself forces the electron to use all its spin and to direct it clockwise or counter-clockwise along the selected axis. Besides, because of the influence we exert on spin when we measure it, we are no more able to define the state of particle before our measurement.

Spin of photons

The case of photons is different: photon spin is not related to any magnetic dipole momentum, but it is connected to the *helicity*: in quantum mechanics spin photon states are called *helicity states*.
It's important to underline that helicity states refer to the direction (+ or −) of a spin component S_i, and not to the total spin vector. For example, let us consider a photon traveling along the direction determined by the z axis. If the photon is in the helicity state $+1$, then it means that its S_z component of the spin vector is positive (and equal to $+\hbar$). Instead, if the photon is in the helicity state -1, then its spin component S_z is negative (and equal to $-\hbar$), i.e. it is in the opposite direction with respect to the propagation direction of the photon.
The case with $S_z = 0$ must be excluded for a photon with null mass.

Appendix B

Antenna parameters

B.1 Definitions

Antennas are characterized by a number of parameters describing their performances. Here a list of the main ones and some definitions necessary when entering in the radio domain.

Radiation pattern

The *antenna radiation pattern* is a graphical representation of the radiation properties of the antenna as a function of space coordinates. In most cases, the radiation pattern is determined in the far field region.
Consider an antenna receiving radio waves from a distant point source. The voltage at the terminals of the antenna as a function of the direction to the point source, normalized to unity at maximum, is called the radiation pattern of the antenna. This pattern is the same regardless of whether it is used as a transmitting antenna or as a receiving antenna, i.e. if it transmits efficiently in some direction, it will also receive efficiently in that direction (this property is called *reciprocity* and follows from Maxwell's equations). A typical power pattern is shown in figure B.1. The power pattern has a primary maximum called the main lobe, several subsidiary maxima called side lobes, and minima called nulls.

Half-Power BeamWidth (HPBW)

The angular width of the beam radiated by high-gain antennas is measured by the *Half-Power Beam Width (HPBW)*, which is the angular separation between the points on the antenna radiation pattern at which the power drops to one-half (-3 dB) its maximum value. Namely, the points at which the main lobe falls to half its central value are called the Half Power points

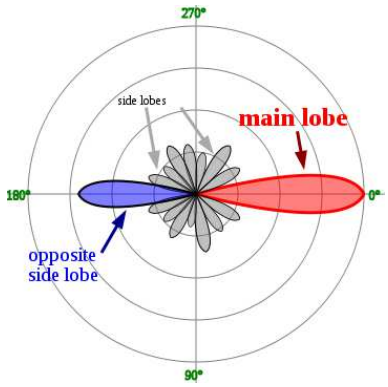

Figure B.1: Typical polar radiation plot, with antenna facing 0°. Most antennae show a pattern of lobes or maxima of radiation. In a directive antenna, shown here, the largest lobe in the desired direction of propagation is called the main lobe. The other lobes are called sidelobes and usually represent radiation in unwanted directions (http://en.wikipedia.org/wiki/Radiation_pattern).

and the angular distance between these points is called the Half Power Beamwidth (figure B.2).

For radio astronomical applications one generally wants the HPBW to

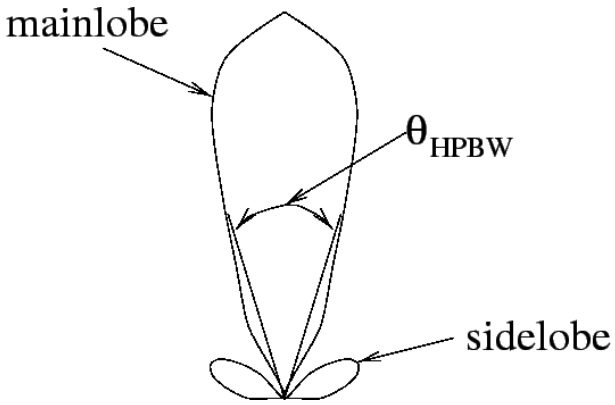

Figure B.2: Schematic power pattern of an antenna, showing the Half-Power Beamwidth (HPBW) (http://www.ncra.tifr.res.in).

be small (so that the nearby sources are not confused with one another), and the sidelobes to be low (to minimize stray radiation). From simple diffraction theory it can be shown that the HPBW of a reflecting telescope is given by $\theta_{HPBW} \sim \lambda/d$ where λ is the wavelength of the radiation and d is the physical dimension of the telescope. So, the larger the telescope, the better the resolution.

For parabolic antennas, the HPBW θ is given by:

$$\theta = \frac{k\lambda}{D} \tag{B.1}$$

where k is a factor which varies slightly depending on the shape of the reflector and the feed illumination pattern. For a typical parabolic antenna $k = 70$ when θ is in degrees.

Gain

Gain is a parameter which measures the degree of directivity of the antenna's radiation pattern. A high-gain antenna will preferentially radiate (and receive) in a particular direction. Specifically, the *antenna gain* is defined as the ratio of the intensity radiated by the antenna in the direction of its maximum output, at an arbitrary distance, divided by the intensity radiated at the same distance by a hypothetical isotropic antenna.
The gain of an antenna is a passive phenomenon, power is not added by the antenna, but simply redistributed to provide more radiated power in a certain direction than would be transmitted by an isotropic antenna.

Near and far field

The near field and the far field of an antenna or other isolated source of electromagnetic radiation are regions around the source, describing the way characteristics of an electromagnetic field change with distance from the source. The basic reason an electromagnetic field changes in character with distance from its source is that Maxwell's equations prescribe different behaviors of electric and magnetic fields, depending on the source terms: electric fields produced by charge distribution have a different character than those produced by the change of magnetic fields. Similarly, Maxwell's equations show a differing behavior for the magnetic fields produced by electric currents, versus magnetic fields produced by the change of electric fields. For these reasons, in the region very close to currents and charge-separations, the electromagnetic field is dominated by electric and magnetic components produced directly by currents and charge-separations, and these effects together produce the electromagnetic *near field*. At distances far from charge-separations and currents, instead, the electromagnetic field becomes dominated by the electric and magnetic fields, one indirectly produced by the change of the other field, and thus it is no longer affected (or much affected) by the charges and currents at the electromagnetic source. This more distant part of the electromagnetic field is called *far field*, or *radiative field*, or *radiation zone*, or *free space*, and it is the familiar type of electromagnetic radiation seen in free space, far from any electromagnetic field sources.
The main characteristics of the *near field* are:

- this field is dominated by the dipole radiation: both currents and the oscillating charge-distributions in antennae (and other radiators) pro-

duce dipole type field behavior, whose intensities may be very powerful near the source, but decay very rapidly with distance in comparison to electromagnetic radiation (far field); strong inductive and capacitative effects from the currents and charges in the antenna cause electromagnetic components not to behave like far field radiation, but these effects decrease in power far more quickly with distance than do the far field radiation effects;

- these non-radiative near field components of electromagnetic fields dominate the electromagnetic field close to the object;

- absorption of radiation does affect the load on the transmitter (magnetic induction can be seen as a very simple model of this type of near field electromagnetic interaction);

- the electric and magnetic fields are nearly independent of each other, and each cannot be calculated from knowing the other (thus, they must be independently measured in the near field), the relationship between E and B becomes very complex; depending on the type of source, the near field will be dominated by either a magnetic component, or an electric component;

- in this close-in region of an antenna, the angular field distribution is dependent upon distance from the antenna;

- all four polarization types (horizontal, vertical, circular, elliptical) can be present.

The main characteristics of the *far field* are, instead:

- this field is dominated by a radiative intensity: the dipole near field intensities, very power near the source, decay very rapidly with distance in comparison to electromagnetic radiation. Radiative far field intensity decays more slowly with distance, following the inverse square law for total electromagnetic power that is typical of all electromagnetic radiation. For this reason, the radiative component of the electromagnetic field wins out in intensity with increasing distance. Indeed, far fields in general fall off in amplitude by $1/r$. This means that the total energy per unit area at a distance r is proportional at $1/r^2$ (instead of $1/r^3$, valid for the dipole radiation). The area of the sphere is proportional to r^2, so the total energy passing through the sphere is constant. This means that the far field energy radiates at infinity;

- electromagnetic radiation, or far field behaviors, dominate at greater distance from the object than the near field components do;

- the far field is the region in which the field acts as "normal" electromagnetic radiation: the power of this radiation decreases as the square of distance from the antenna, and absorption of the radiation has no effect on the transmitter;

- because each component (electric and magnetic) of the electromagnetic field in the far field region is generated by a change in the other component, the ratios of electric to magnetic field strength are fixed and unvarying;

- the antenna radiation pattern is independent of distance from the source;

- electromagnetic waves are usually characterized by a single polarization type (horizontal, or vertical, or circular, or elliptical).

The boundaries for these regions are approximate as there are no precise cutoffs between them (all behavioral changes with distance are smooth changes), and experts may differ in their definitions describing these regions. The near field does not suddenly end where the far field begins, rather there is a *transition zone* between these fields where both types of electromagnetic field effects may be significant. In this region, near field behavior dies out and ceases to be important, leaving far field effects as dominant interactions.
There are different definitions about the boundaries for these regions. One way to define them is associated to the dimension of the antenna with respect to the dominant wavelength, λ.
For *electromagnetically short antennae*, i.e. for antennae shorter than half of the wavelength of the radiation they emit, the far and near regional boundaries are measured in terms of simple ratio of the distance from the radiating source, r, to the wavelength of the radiation. Indeed, for such an antenna, the near field is the region within a radius $r << \lambda$, while the far field is the region for which $r >> 2\lambda$. Note that the dimension of the antenna, is not important and the approximation is the same for all shorter antennae (sometimes ideally called "point antennae").
For *electromagnetically long antennae*, i.e. antennae physically larger than a half-wavelength of the radiation they emit, the near and far field are defined in terms of the the Fraunhofer or Rayleigh distance d_R:

$$d_R = 2\frac{D^2}{\lambda} \tag{B.2}$$

where D is the largest dimension of the radiator, and corresponds to the physical length of an antenna, or the diameter of a dish antenna. This distance provides the limit between the near and far field.

Bibliography

[1] V. M. Abraham, *Der drehimpuls des lichtes*, Physik. Zeitschr. **XV**, 1914.

[2] L. Allen, M. W. Beijersbergen, R. J. C. Spreeuw, and J. P. Woerdman, *Orbital angular momentum of light and the transformation of laguerre-gaussian laser modes*, Phys. Rev. A **45** (1992), 8185.

[3] L. Allen and M. J. Padgett, *The poynting vector in laguerre-gaussian beams and the interpretation of their angular momentum density*, Optics Communications **184** (2000), 67.

[4] M. F. Andersen, C. Ryu, Pierre Cladé, Vasant Natarajan, A. Vaziri, K. Helmerson, and W. D. Phillips, *Quantized rotation of atoms from photons with orbital angular momentum*, Phys. Rev. Lett. **97** (2006), 170406.

[5] P. W. Anderson, *Plasmons, gauge invariance, and mass*, Phys. Rev. **130** (1963), 439.

[6] F. T. Arecchi, G. Giacomelli, P. L. Ramazza, and S. Residori, *Vortices and defect statistics in two-dimensional optical chaos*, Phys. Rev. Lett. **67** (1991), 3749.

[7] M. Babiker, W. L. Power, and L. Allen, *Light-induced torque on moving atoms*, Phys. Rev. Lett. **73** (1994), 1239.

[8] C. Barbieri, F. Tamburini, G. Anzolin, A. Bianchini, E. Mari, A. Sponselli, G. Umbriaco, M. Prasciolu, F. Romanato, and P. Villoresi, *Light's orbital angular momentum and optical vortices for astronomical coronography from ground and space telescopes*, Earth, Moon, and Planets **105** (2009), no. 2-4, 283.

[9] S. M. Barnett and L. Allen, *Orbital angular momentum and nonparaxial light beams*, Opt. Commun. **110** (1994), 670.

[10] V. Bazhenov, M. Soskin, and M. Vasnetsov, *Screw dislocations in light wave-fronts*, J. Mod. Opt. **39** (1992), 985.

[11] V. Y. Bazhenov, M. V. Vasnetsov, and M. S. Soskin, *Laser beams with screw dislocations in their wavefronts*, JETP Lett. **52** (1990), 429.

[12] M. W. Beijersbergen, R. P. C. Coerwinkel, and J. P. Woerdman M. Kristensen, *Helical-wavefront laser beams produced with a spiral phaseplate*, Opt. Commun. **112** (1994), 321.

[13] V. B. Berestetskii, E. M. Lifshitz, and L. P. Pitaevskii, *Quantum electrodynamics*, 2nd ed., vol. 4, Oxford: Butterworth-Heinemann, 1982.

[14] G. C. G. Berkhout and M. W. Beijersbergen, *Method for probing the orbital angular momentum of optical vortices in electromagnetic waves from astronomical objects*, Phys. Rev. Lett. **101** (2008), 100801.

[15] G. C. G. Berkhout, M. P. J. Lavery, J. Courtial, M. W. Beijersbergen, and M. J. Padgett, *Efficient sorting of orbital angular momentum states of light*, Phys. Rev. Lett. **105** (2010), 153601.

[16] G. C. G. Berkhout, M. P. J. Lavery, M. J. Padgett, and M. W. Beijersbergen, *Measuring orbital angular momentum superpositions of light by mode transformation*, Optics Letters **36** (2011), no. 10, 1863.

[17] Gregorius C. G. Berkhout, *Fundamental methods to measure the orbital angular momentum of light*, Doctoral thesis, Leiden Institute of Physics, Leiden University, 2011.

[18] M. V. Berry, *Paraxial beams of spinning lights*, Singular Optics (Eds. M.S. Soskin and M.V. Vasnetsov) SPIE 3487, 1998.

[19] ———, *Making waves in physics*, Nature **403** (2000), 21.

[20] R. A. Beth, *Mechanical detection and measurement of the angular momentum of light*, Phys. Rev. Lett. **50** (1936), 115.

[21] G. F. Brand, *Phase singularities in beams*, American Journal of Physics **67** (1999), no. 1, 55.

[22] J. Courtial, D. A. Robertson, K. Dholakia, L. Allen, and M. J. Padgett, *Rotational frequency shift of a light beam*, Phys. Rev. Lett. **81** (1998), 4828.

[23] N. M. Elias, *Photon orbital angular momentum in astronomy*, Astron. Astrophys. **492** (2008), 883.

[24] G. Foo, D. M. Palacios, and Grover A. Swartzlander Jr., *Optical vortex coronagraph*, Optics Letters **30** (2005), no. 24, 3308.

[25] S. Franke-Arnold, L. Allen, and M. Padgett, *Advances in optical angular momentum*, Laser & Photon. Rev. **2** (2008), no. 4, 299.

[26] M. E. J. Friese, J. Enger, H. Rubinsztein-Dunlop, and N. R. Heckenberg, *Optical angular-momentum transfer to trapped absorbing particles*, Phys. Rev. A **54** (1996), no. 2, 1593.

[27] D. P. Ghai, P. Senthilkumaran, and R. S. Sirohi, *Single-slit diffraction of an optical beam with phase singularity*, Optics and Lasers in Engineering **47** (2009), no. 1, 123.

[28] G. Gibson, J. Courtial, M. J. Padgett, M. Vasnetsov, V. Pas'ko, S. M. Barnett, and S. Franke-Arnold, *Free-space information transfer using light beams carrying orbital angular momentum*, Opt. Express **12** (2004), 5448–5456.

[29] A. S. Goldhaber and M. M. Nieto, *Photon and graviton mass limits*, Rev. Mod. Phys. **82** (2010), 939.

[30] D. G. Grier, *A revolution in optical manipulation*, Nature **482** (2003), 810.

[31] M. Harwit, *Photon angular momentum in astrophysics*, The Astrophysical Journal **597** (2003), 1266.

[32] H. He, M. E. J. Friese, N. R. Heckenberg, and H. Rubinsztein-Dunlop, *Direct observation of transfer of angular momentum to absorptive particles from a laser beam with a phase singularity*, Phys. Rev. Lett. **75** (1995), 826.

[33] N. Heckenberg, R. McDuff, C. Smith, and A. White, *Generation of optical phase singularities by computer-generated holograms*, Opt. Lett. **17** (1992), 221.

[34] N. R. Heckenberg, R. McDuff, C. P. Smith, H. Rubinsztein-Dunlop, and M. J. Wegener, *Laser beams with phase singularities*, Opt. Quantum Electron. **24** (1992), S951.

[35] W. Heitler, *The quantum theory of radiation*, 3rd ed., The International Series of Monographs on Physics, Clarendon Press, Oxford, 1954.

[36] J. M. Hickmann, E. J. S. Fonseca, W. C. Soares, and S. Chávez-Cerda, *Unveiling a truncated optical lattice associated with a triangular aperture using light's orbital angular momentum*, Phys. Rev. Lett. **105** (2010), 053904.

[37] H. Hora, *Plasmas at high temperature and density*, Springer, 1991.

[38] J. D. Jackson, *Classical electrodynamics*, 3rd ed., Wiley & Sons, New York, NY, 1999.

[39] J. M. Jauch and F. Rohrlich, *The theory of photons and electrons*, Springer-Verlag, Reading, MA, 1980.

[40] G. A. Swartzlander Jr., *The optical vortex coronograph*, Journal of Optics A: Pure Appl. Opt. **11** (2009), 094022.

[41] G. A. Swartzlander Jr., E. L. Ford, R. S. Abdul-Malik, L. M. Close, M. A. Peters, D. M. Palacios, and D. W. Wilson, *Astronomical demonstration of an optical vortex coronagraph*, Optics Express **16** (2008), no. 14, 10200.

[42] Y. S. Kivshar and E. A. Ostrovskaya, *Optical vortices: Folding and twisting waves of light*, Optics & Photonics News **12** (2001), no. 4, 24.

[43] M. P. J. Lavery, G. C. G. Berkhout, J. Courtial, and M. J. Padgett, *Measurement of the light orbital angular momentum spectrum using an optical geometric transformation*, J. Opt. **13** (2011), 064006.

[44] M. P. J. Lavery, D. J. Robertson, G. C. G. Berkhout, G. D. Love, M. J. Padgett, and J. Courtial, *Refractive elements for the measurement of the orbital angular momentum of a single photon*, Optics Express **20** (2012), no. 3, 2110.

[45] J. Leach, M. J. Padgett, S. M. Barnett, S. Franke-Arnold, and J. Courtial, *Measuring the orbital angular momentum of a single photon*, Phys. Rev. Lett. **88** (2002), 257901.

[46] J. H. Lee, G. Foo, E. G. Johnson, and G. A. Swartzlander Jr., *Experimental verification of an optical vortex coronograph*, Phys. Rev. Lett. **97** (2006), 053901.

[47] A. Mair, A. Vaziri, G. Weihs, and A. Zeilinger, *Entanglement of the orbital angular momentum states of photons*, Nature **412** (2001), 313.

[48] M. Malik, M. O'Sullivan, B. Rodenburg, M. Mirhosseini, J. Leach, M. P. J. Lavery, M. J. Padgett, and R. W. Boyd, *Influence of atmospheric turbulence on optical communications using orbital angular momentum for encoding*, Opt. Express **20** (2012), no. 12, 13195.

[49] E. Mari, G. Anzolin, F. Tamburini, M. Prasciolu, G. Umbriaco, A. Bianchini, C. Barbieri, and F. Romanato, *Fabrication and testing of $l = 2$ optical vortex phase masks for coronography*, Optics Express **18** (2010), no. 3, 2339.

[50] L. Marrucci, C. Manzo, and D. Paparo, *Optical spin-to-orbital angular momentum conversion in inhomogeneous anisotropic media*, PRL **96** (2006), 163905.

[51] L. Marucci, E. Karimi, S. Slussarenko, B. Piccirillo, E. Santamato, E. Nagali, and F. Sciarrino, *Spin-to-orbital conversion of the angular momentum of light and its classical and quantum applications*, J. Opt. **13** (2011), 064001.

[52] J.C. Maxwell, *A treatise on electricity and magnetism*, Oxford: Clarendon Press, Art. 793, 1881.

[53] J. T. Mendonça, *Theory of photon acceleration*, IoP (Institute of Physics Publishing Bristol and Philadelphia), ISBN 0-7503-0711-0, 2001.

[54] J. T. Mendonça, S. Ali, and B. Thidé, *Plasmons with orbital angular momentum*, Phys. Plasmas **16** (2009), 112103.

[55] J. T. Mendonça, B. Thidé, J. E. S. Bergman, S. M. Mohammadi, B. Eliasson, W. Baan, and H. Then, *Photon orbital angular momentum in a plasma vortex*, arXiv:0804:3221 (2008).

[56] G. Molina-Terriza, *Multipolar expansion of orbital angular momemtum modes*, arXiv:0804.1494v1, 2008.

[57] G. Molina-Terriza, J. P. Torres, and L. Torner, *Twisted photons*, Nature Phys. **3** (2007), 305.

[58] A. T. Ò Neil, I. MacVicar, L. Allen, and M. J. Padgett, *Intrinsic and extrinsic nature of the orbital angular momentum of a light beam*, Phys. Rev. Lett. **88** (2002), 053601.

[59] S. S. Oemrawsingh, J. de Jong, X. Ma, and A. Aiello, *High-dimensional mode analyzers for spatial quantum entranglement*, Phys. Rev. A **73** (2006), 032339.

[60] D. W. Oesch and D. J. Sanchez, *Creating well-defined orbital angular momentum states with a random turbulent medium*, Opt. Express **20** (2012), 12292.

[61] M. Padgett and R. Bowman, *Tweezers with a twist*, Nature Photonics **5** (2011), 343.

[62] M. J. Padgett and L. Allen, *The poynting vector in laguerre-gaussian laser modes*, Optics Communications **121** (1995), 36.

[63] M. J. Padgett, J. Arlt, N. Simpson, and L. Allen, *An experiment to observe the intensity and phase structure of laguerre-gaussian laser modes*, Am. J. Phys. **64** (1996), 77.

[64] D. M. Palacios, I. D. Maleev, A. S. Marathay, and G.A. Swartzlander Jr., *Spatial correlation singularity of a vortex field*, Phys. Rev. Lett. **92** (2004), 143905.

[65] C. Paterson, *Atmospheric turbulence and orbital angular momentum of single photons for optical communications*, Phys. Rev. Lett. **94** (2005), 153901.

[66] Poynting, *The wave motion of a revolving shaft, and a suggestion as to the angular momentum in a beam of circularly polarised light*, Proc. Roy. Soc. London Ser. A **82** (1909), 560.

[67] J. H. Poynting, *On the transfer of energy in the electromagnetic field*, Phil. Trans. **175** (1884), 343.

[68] B. Rodenburg, M. P. J. Lavery, M. Malik, M. N. O'Sullivan, M. Mirhosseini, D. J. Robertson, M. J. Padgett, and R. W. Boyd, *Influence of atmospheric turbulence on states of light carrying orbital angular momentum*, Optics Letters **37** (2012), no. 17, 3735.

[69] D. J. Sanchez and D. W. Oesch, *The localization of angular momentum in optical waves propagating through atmospheric turbulence*, Opt. Express **19** (2011), 25388.

[70] ———, *Orbital angular momentum in optical waves propagating through distributed atmospheric turbulence*, Opt. Express **19** (2011), 24596.

[71] J. Schwinger, *Gauge invariance and mass*, Phys. Rev. **125** (1988), 397.

[72] J. Schwinger, L. L. DeRaad jr., K. A. Milton, and W. Tsai, *Classical electrodynamics*, Perseus Books Reading, Mass, ISBN:0-7382-0056-5, 1998.

[73] N. B. Simpson, K. Dholakia, L. Allen, and M. J. Padgett, *Mechanical equivalence of spin and orbital angular momentum of light: An optical spanner*, Optics Letters **22** (1997), no. 1, 52.

[74] M. S. Soskin, V. N. Gorshkov, M. V. Vasnetsov, J. T. Malos, and N. R. Heckenberg, *Topological charge and agular momentum of light beams carrying optical vortices*, Phys. Rev. A **56** (1997), 4064.

[75] A. M. Stewart, *Angular momentum of the electromagnetic field: The plane wave paradox resolved*, Eur. J. Phys. **26** (2005), 635.

[76] H. I. Sztul and R. R. Alfano, *Double-slit interference with laguerre-gaussian beams*, Optics Letters **31** (2006), no. 7, 999.

[77] F. Tamburini, G. Anzolin, A. Bianchini, and C. Barbieri, *Overcoming the rayleigh criterion limit with optical vortices*, Phys. Rev. Lett. **97** (2006), 163903.

[78] F. Tamburini, E. Mari, A. Sponselli, B. Thidé, A. Bianchini, and F. Romanato, *Encoding many channels on the same frequency through radio vorticity: First experimental test*, New J. Phys. **14** (2012), 033001.

[79] F. Tamburini, E. Mari, B. Thidé, C. Barbieri, and F. Romanato, *Experimental verification of photon angular momentum and vorticity with radio techniques*, Appl. Phys. Lett. **99** (2011), 204102.

[80] F. Tamburini, A. Sponselli, B. Thidé, and J. T. Mendoça, *Photon orbital angular momentum and mass in a plasma vortex*, EPL **90** (2010), 45001.

[81] F. Tamburini, B. Thidé, G. Molina-Terriza, and G. Anzolin, *Twisting of light around rotating black holes*, Nature Phys. **7** (2011), 195.

[82] F. Tamburini, G. Umbriaco, G. Anzolin, C. Barbieri, and A. Bianchini, *Frogeye, the quantum coronagrapic mask. the photon orbital angular momentum and its applications to astronomy*, Mem. S.A.It. Suppl. **9** (2006), 484.

[83] F. Tamburini and D. Vicino, *Photon wave function: A covariant formulation and equivalence with qed*, Phys. Rev. Lett. **78** (2008), 052116.

[84] B. Thidé, *Nonlinear physics of the ionosphere and lois/lofar*, Plasma Phys. Control. Fusion **49** (2007), B103.

[85] ———, *Electromagnetic field theory*, 2nd ed., On-Line Textbook (http://www.plasma.uu.se/CED/Book/, 2011.

[86] B. Thidé, H. Then, J. Sjöholm, K. Palmer, J. Bergman, T. D. Carozzi, Ya.N. Istomin, N. H. Ibragimov, and R. Khamitova, *Utilization of photon orbital angular momentum in the low-frequency radio domain*, Phys. Rev. Lett. **99** (2007), 087701.

[87] T. Tolonen and M. Karjalainen, *A computationally efficient multipitch analysis model*, IEEE Trans. Speech Audio Process. **8** (2000), 708.

[88] Juan P. Torres and Lluis Torner (editors), *Twisted photons,applications of light with orbital angular momentum*, WILEY-VHC, 2011.

[89] G. A. Turnbull, D. A. Robertson, G. M. Smith, L. Allen, and M. J. Padgett, *The generation of free-space laguerre-gaussian modes at millimetre-wave frequencies by use of a spiral phaseplate*, Optics Communications **127** (1995), 183.

[90] N. Uribe-Patarroyo, A. Alvarez-Herrero, A. López Ariste, A. Asensio Ramos, T. Belenguer, R. Manso Sainz, C. LeMen, and B. Gelly, *Detecting photons with orbital angular momentum in extended astronomical objects: Application to solar observations*, Astrnomy & Astrophysics **526** (2011), A56.

[91] S. J. van Enk and G. Nienhuis, *Spin and orbital angular momentum of photons*, Europhys. Lett. **25** (1994), 497.

[92] M. V. Vasnetsov, V. A. Pas'ko, and M. S. Soskin, *Analysis of orbital angular momentum of a misaligned optical beam*, Nwe Journal of Physics **7** (2005), 46.

[93] A. Vaziri, G. Weihs, and A. Zeilinger, *Superpositions of the orbital angular momentum for applications in quantum experiments*, J. Opt. B: Quantum Semiclass. Opt. **4** (2002), 47.

[94] A. M. Yao and M. J. Padgett, *Orbital angular momentum: Origins, behavior and applications*, Advances in Optics and Photonics **3** (2011), 161.